



Institute for Geophysics, Astrophysics, and Meteorology
University of Graz

Atmospheric Remote Sensing and Climate System Research Group
ARSCliSys – on the art of understanding the climate system



IGAM/UG Technical Report for ESA/ESTEC No. 1/2002

ESA study:

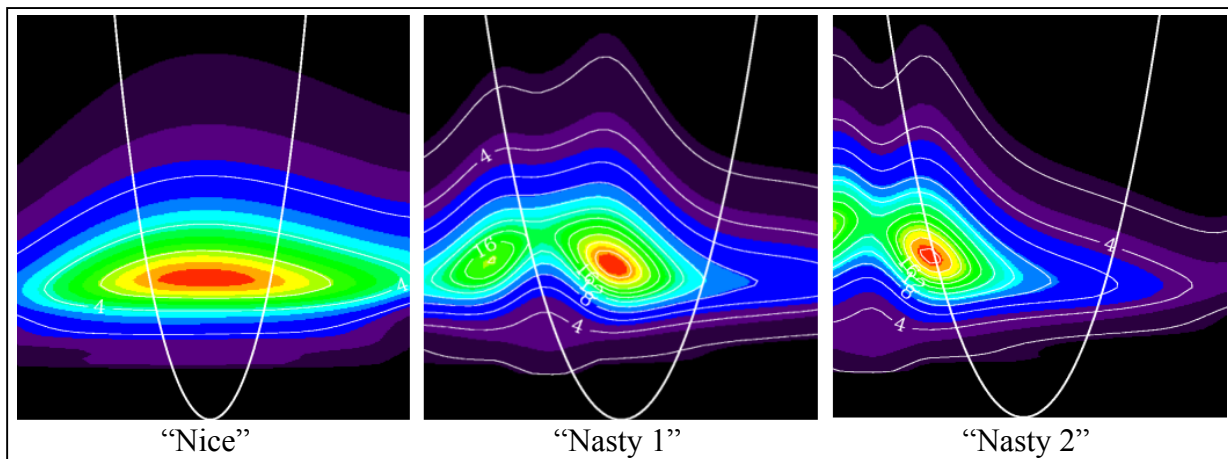
ACE Scientific Support Study

[ESA/ESTEC Contract No. 14809/00/NL/MM, WP3000: Error Analysis for Climate Applications; Part WP3200]

Sensitivity of Atmospheric Profiles Retrieved from GNSS Occultation Data to Ionospheric Residual and High-Altitude Initialization Errors

by

A. Gobiet and G. Kirchengast
(IGAM/University of Graz, Graz, Austria)



January 2002

(page intentionally left blank; back-page if double-sided print)

Table of Contents

1 INTRODUCTION	1
2 IONOSPHERIC CORRECTION AND STATISTICAL OPTIMIZATION	2
2.1 Ionospheric correction	2
2.2 Statistical optimization	3
3 STUDY SETUP	5
3.1 The EGOPS software tool	6
3.2 Atmospheric models	7
3.3 Satellite mission simulation	8
3.4 The three representative occultation events	9
3.4.1 Geometrical properties	9
3.4.2. Ionospheric conditions	10
4. RESULTS	14
4.1 The effects of statistical optimization	16
4.2 The effects of ionization level and ionospheric symmetry	18
4.3 Interaction between ionospheric residuals and statistical optimization	21
4.4 Residuals in the troposphere and lower stratosphere	22
5. CONCLUSION AND OUTLOOK	22
REFERENCES	24
APPENDIX A. RETRIEVAL RESULTS – REALISTIC RECEIVING SYSTEM	27
A.1. Bending Angle	28
A.2. Refractivity	31
A.3. Pressure	34
A.4. Geopotential Height	37
A.5. Temperature	40

APPENDIX B. RETRIEVAL RESULTS – IDEAL RECEIVING SYSTEM	43
B.1. Bending Angle	44
B.2. Refractivity	47
B.3. Pressure	50
B.4. Geopotential Height	53
B.5. Temperature	56

1 Introduction

This report is part of Work Package 3000 (WP 3000) of the ACE Scientific Support Study (Hoeg et al., 2000). WP 3000 is dedicated to the error analysis of Global Navigation Satellite System (GNSS) radio occultation (RO) measurements for climate applications. Here we report on the work performed under work package part 3200 (WP 3200) focusing on ionospheric residual errors and high-altitude initialization errors.

The primary observable of RO measurements is the phase delay of a GNSS signal passing through the Earth’s atmosphere. From the phase delay the Doppler shift and subsequently the total bending angle can be deduced. All other products, such as refractivity, pressure, geopotential height, temperature and water vapor, are derived from the total bending angle (e.g., Melbourne et al, 1994; Kursinski et al, 1997; Steiner et al., 1999). Close to the surface, the bending angle depends mostly on the contribution of the neutral atmosphere, above 45 km the contribution of the ionosphere starts to dominate (e.g., Hocke, 1997).

In order to retrieve neutral atmosphere parameters, it is necessary to remove the ionospheric contribution to the signal. Since the errors of these parameters at some altitude depend on the bending angle errors above that altitude, accurate “ionosphere-free” bending angles to as high altitudes as possible are desirable. There are several methods to remove the ionospheric contribution from the signal (e.g., Syndergaard, 2000; more information in section 2.1). In recent applications the method of linear correction of bending angles (Vorob’ev and Krasnil’nikova, 1994; more information in section 2.1) has been the method of choice.

Whatever processing applied, the retrievals at heights above about 30 km, i.e., in the upper stratosphere, are sensitive to residual ionospheric noise and measurement noise. This calls for sensible use of the data at high altitudes, in particular above the stratopause, where the signal-to-noise ratio is low. “Statistical optimization” can be applied to smooth bending angles at high altitudes, a concept initially introduced by Sokolovskiy and Hunt (1996). Various implementations of this approach exist, all combining measured bending angle profiles with background bending angle profiles, usually from climatological models. By this means the initialization at high altitudes is enhanced in order to mitigate errors in subsequent retrieval steps. Section 2.2 summarizes the most common high-altitude initialization methods used so far.

The objective of sub-work package 3200 (WP 3200) was to analyze the sensitivity of RO retrieval products to ionospheric residual errors and to high-altitude initialization errors, respectively. Furthermore it was attempted to reveal aspects of the interaction of these two error sources. After briefly summarizing the methodologies in use for ionospheric correction and statistical optimization in section 2, the study setup is described in section 3. In section 4 we then report on the results, and in section 5 the main conclusions are drawn and some aspects worth further study are highlighted. Finally, appendices are available (Appendix A and B), which serve as in-depth information source on the detailed results for all retrieval products investigated (bending angle, refractivity, pressure, geopotential height, and temperature).

2 Ionospheric correction and statistical optimization

2.1 Ionospheric correction

The ionosphere, as an dispersive medium, leads to different phase delays of the two GNSS signals (Φ_1 for the L1 signal and Φ_2 for the L2 signal) as well as to different L1 and L2 ray paths. This dispersion effect can be used for a first-order removal of ionospheric effects on the signals. The two most important linear correction methods for the removal of the ionospheric contribution are:

Linear correction of phases:

$$\Phi_{LC}(t) = \frac{f_1^2 \Phi_1(t) - f_2^2 \Phi_2(t)}{f_1^2 - f_2^2} \quad (1)$$

f_1, f_2 : carrier frequencies of L1 and L2 signals, respectively

t : time

Φ_{LC} : linearly corrected phase delay

Linear correction of bending angles:

$$\alpha_{LC}(a) = \frac{f_1^2 \alpha_1(a) - f_2^2 \alpha_2(a)}{f_1^2 - f_2^2} \quad (2)$$

α_1, α_2 : bending angles derived at L1 and L2, respectively

a : impact parameter

α_{LC} : linearly corrected bending angle

The linear correction of bending angles (Vorob'ev and Krasnil'nikova, 1994) provides in general significantly better results than the linear correction of phases (e.g., Spilker, 1980), since it accounts for the different ray paths of L1 and L2 by using the same impact parameter (instead of the same time). Moreover, it exploits the fact that most of the total bending angle is accumulated near the ray perigee in the atmosphere. This was shown by several theoretical and simulation studies (Vorob'ev and Krasnil'nikova, 1994; Ladreiter and Kirchengast, 1996; Hocke et al., 1997).

There are some methods that account for higher-order effects of the ionosphere on RO signals (Syndergaard, 2000; Gorbunov et al., 1996), but they rely on additional a priori data and have not been evaluated in quasi-realistic studies yet. Since the linear correction of bending angles has become the method of choice in recent years, it was used in this study to remove the contribution of the ionosphere to the simulated occultation measurements.

2.2 Statistical optimization

As indicated in the introduction, RO-measurements are sensitive to ionospheric residual noise and various components of observation system related noise at altitudes above 30 km. The statistical optimization approach attempts to find the most probable bending angle profile by combining an observed bending angle profile with a (usually smooth) background bending angle profile (“a priori-profile”, usually from climatology) in a statistically optimal way. This concept was introduced by Sokolovskiy and Hunt (1996) into the context of GNSS RO retrievals. In general form, the optimization formula can be written as:

$$\alpha_{opt} = \alpha_b + \mathbf{B}(\mathbf{B} + \mathbf{O})^{-1}(\alpha_o - \alpha_b) \quad (3)$$

- α_{opt} : most probable bending angle profile
- α_o : observed bending angle profile (ionosphere-corrected)
- \mathbf{O} : observation error covariance matrix
- α_b : background (a priori) bending angle profile (from climatology)
- \mathbf{B} : background error covariance matrix

The general effect of this modification (or “smoothing”) of the observed bending angle profile can be described as follows: At higher altitudes, where the ionospheric residual error and the other noise components exceed the error of the a priori profile from climatology, α_{opt} will be determined by climatology. At lower altitudes, where the climatology error becomes dominant, α_{opt} will be determined by the observed data. It should be noted that statistical optimization does not improve the quality of observed profiles themselves at high altitudes, but rather delivers an improved combined profile, thanks to the climatological information invoked. The most important effect is, however, that the optimization minimizes error propagation downwards to altitudes, where observed data have a good signal-to-noise ratio.

Since the *inverse covariance weighting* approach, Eq. (3), faces the difficulty of requiring accurate covariance matrices, which are not so easy to define properly, Sokolovskiy and Hunt (1996) demonstrated this technique by using a simpler form, assuming vertically uncorrelated errors (i.e., all non-diagonal elements of the error covariance matrices are zero). For the individual bending angles at any height z this simplified *inverse variance weighting* approach can be written as:

$$\alpha_{opt}(z) = \alpha_b(z) + \frac{\sigma_b^2(z)}{\sigma_b^2(z) + \sigma_o^2(z)}(\alpha_o(z) - \alpha_b(z)) \quad (4)$$

- $\sigma_o^2(z)$: variance of the observed bending angle (usually estimated from $\sigma_o(z)$ at $z > 70$ km)
- $\sigma_b^2(z)$: variance of the background bending angle (usually obtained via $\sigma_b(z) = 0.2 \alpha_b(z)$)

Equation (4) was also applied by Gorbunov and Gurvich (1998). An alternative expression is given by the *heuristic* approach (Hocke *et al*, 1997; Hocke, 1997; Steiner *et al*, 1999):

$$\alpha_{opt}(z) = \alpha_b(z) + \frac{\sigma_b(z)}{\sigma_b(z) + \sigma_o(z)} (\alpha_o(z) - \alpha_b(z)) \quad (5)$$

Heuristic means in this context that though the optimization is formally based on the theory of Gaussian random processes, the actual variance estimation does, for the sake of practical advantages, not strictly follow this theory. As Eq. (5) shows, the weighting uses standard deviations instead of the variances and, in addition, the heuristic estimate $\sigma_o(z) = |\alpha_o(z) - \alpha_b(z)|$ is adopted for the observed standard deviation (e.g., Hocke, 1997); $\sigma_b(z)$ is again set to express 20% uncertainty (cf. Eq. (4)). The heuristic approach is simple to implement ray by ray, and can better cope with more noisy data than the inverse variance weighting approach, Eq. (4). It leads, in a formal statistical sense, to a non-optimal combined profile, however.

Healy (2001) suggested to use the full inverse covariance weighting approach, Eq. (3), with a simplified analytical background (a priori) error covariance matrix formulated as:

$$\mathbf{B}_{ij} = \sigma_i \sigma_j \exp\left(-\frac{(a_i - a_j)^2}{l^2}\right) \quad (6)$$

a_i, a_j : i th and j th impact parameter values
 l : error correlation length (usually $l = 6$ km)

The observed bending angle errors have still been assumed to be vertically uncorrelated by Healy (2001). Since observation errors mainly contain noise, this assumption is valid to a much higher degree than for the errors of the climatological a priori profile.

The most advanced optimization concept proposed so far has been discussed by Rieder and Kirchengast (2001), who generalized the treatment of the optimization problem to employ the full breath of the optimal estimation methodology introduced by Rodgers (1976; 1990; 2000). This general treatment is not specifically focused on bending angle optimization but the a priori information can be fused in at any retrieval product level (e.g., bending angle, refractivity, temperature) desired by the scientific user.

It has been shown that statistical optimization approaches can significantly improve the quality of the RO retrieval (e.g., Steiner *et al.*; 1999). Nevertheless, the quality achieved is highly dependent on the quality of the a priori profiles as, for example, shown by Healy (2001). Syndergaard (*priv. communications*, 1999) suggested to perform bending angle profile search prior to statistical optimization, i.e., to fit many (or some selected) available bending angle profiles from climatology to the observed profile by the method of least squares and subsequently use the best-fit profile instead of the geographically co-located profile as the a priori profile in the statistical optimization process.

The latter concept is implemented in the “high-end” statistical optimization algorithm used in this study, including bending angle search over the complete domain of climatological profiles available in the MSIS climatological model (Hedin, 1991) as well as full exploitation of the inverse covariance weighting approach with proper non-diagonal covariance matrices for both **O** and **B**.

In total, we compared in this study the performance of three different high-altitude initialization methods, two of them employing statistical optimization:

- *No optimization*: In this classical early approach (see, e.g., Kursinski *et al.*, 1997) an upper boundary height is selected – at altitudes between 50 and 70 km, depending on signal-to-noise ratio – above which an extrapolated exponential bending angle profile is used, the extrapolation being based on an exponential fit to the data in the last ~10 km beneath the upper boundary height. Below this boundary height, also called initialization height, direct use is made of the observed bending angle profile. This traditional approach features several distinct weaknesses compared to statistical optimization, most importantly the sensitivity of the initial height selection and of extrapolation quality to the noise in the data as well as the intrinsic assumption of an isothermal atmosphere above the initialization height.
- *Heuristic optimization*: Eq. (5) is used to optimize the observed bending angle profile by fusing in the geographically co-located MSIS profile as a priori profile (i.e., approach of Hocke *et al.*, 1997).
- *Inverse covariance weighting optimization*: Here the “high end” algorithm outlined in the previous paragraph is used, which is the most advanced algorithm available so far (developed at IGAM/University of Graz, details not yet published).

3 Study setup

The study was performed using a systematic case study design. We chose three occultation events as base scenarios (see section 3.4), each of them being representative for one type of symmetry (or asymmetry) of the electron density distribution in the ionosphere (see section 3.4.2). In order to study the residual errors from ionospheric correction and the effects of statistical optimization as a function of ionospheric state, we simulated the propagation of the GNSS signal through the atmosphere (“forward modeling”) both without ionosphere (“no ionosphere” case) and at three different ionization levels, represented by the radio flux at 10.7 cm ($F_{10.7}$ -index): low ionization ($F_{10.7} = 70$), moderate ionization ($F_{10.7} = 140$), and high ionization ($F_{10.7} = 210$), respectively. The “no ionosphere” case serves as a convenient reference case, the three different ionization levels well reflect the typical state of the ionosphere under low, middle, and high solar activity conditions, respectively.

For all these forward-modeled scenarios, we simulated two different types of receiving systems: The “realistic receiving system” including error sources like orbit uncertainties, receiver noise, local multipath errors and clock errors, and the “ideal receiving system” ignoring all the error sources mentioned above (i.e., assuming no observation system-related errors). For the realistic receiving system simulation, we reflected (conservatively) the specifications and error characteristics of the GRAS instrument (e.g., GRAS-SAG, 1998).

Subsequently, we performed the RO retrieval for all simulated occultation events using the three different statistical optimization approaches introduced in section 2.2: no optimization (with observed profile exponentially extrapolated), heuristic optimization (with co-located a priori profile), and inverse covariance weighting optimization (with a priori profile search), respectively.

The results are presented as absolute error profiles for the geopotential height and the temperature and as relative error profiles for the other retrieval products (bending angle, refractivity and pressure) between surface and 60 km height. In the present context, error means the (relative) deviation of a retrieved value from the “true” atmospheric value at the

occultation tangent point as provided by the neutral atmosphere used in the forward modeling (see section 3.2). The “true” bending angle profiles were extracted directly from the 3D ray-tracing algorithm employed to simulate the phase delay measurements.

We also quantified, to provide some simple scalar quality indicator, the average error of each profile between 35 and 45 km. We did this by calculating the bias, which describes the mean deviation of the retrieved profile from the “true” profile in this height interval, and the standard deviation (stddev), which describes the fluctuation of the (bias-corrected) error profile in the same interval. These two values are depicted at the top of each error profile panel in the result figures.

For the interpretation of the results we mainly made use of the retrieved temperatures (see section 4). A comprehensive compilation of all retrieval products is given in the two appendices (Appendix A and B).

The complete study, beginning with satellite mission planning and simulation, proceeding with modeling of GNSS signal propagation through the atmosphere/ionosphere, simulation of the observation system, retrieval of the observables, and analysis of the results was realized by means of the EGOPS software tool, a simulation system which is briefly described in the following subsection.

3.1 The EGOPS software tool

The EGOPS (End-to-end GNSS Occultation Performance Simulator) is a largely ESA-funded software tool developed as an international European effort under the leadership of the IGAM/University of Graz (Kirchengast, 1998; Kirchengast *et al.*, 2001).

EGOPS is capable of an integrated simulation of the GNSS based radio occultation technique in an end-to-end manner from the GNSS satellites transmitting the signals down to final data products like atmospheric profiles of temperature and water vapor. The tool can also be used to process real occultation data. The major objectives of EGOPS are:

- (i) Mission analysis and planning for low Earth orbit (LEO) satellites equipped with GNSS occultation receivers and for GNSS scatterometry (geometry of events, coverage by events, various statistics for GNSS/LEO/ground station constellations, etc.),
- (ii) Simulation of spaceborne or airborne occultation observations (forward modeling through the atmosphere-ionosphere system and observation system modeling such as of signal tracking and noise sources),
- (iii) Processing of simulated or observed occultation data (inversion from phase and amplitude observables to atmospheric/ionospheric profiles by a variety of different processing chains),
- (iv) integrated post-processing, visualization, validation, and documentation of all simulator results (interactive exploration in form of statistics, geographic maps, profiles, data animations, etc.).

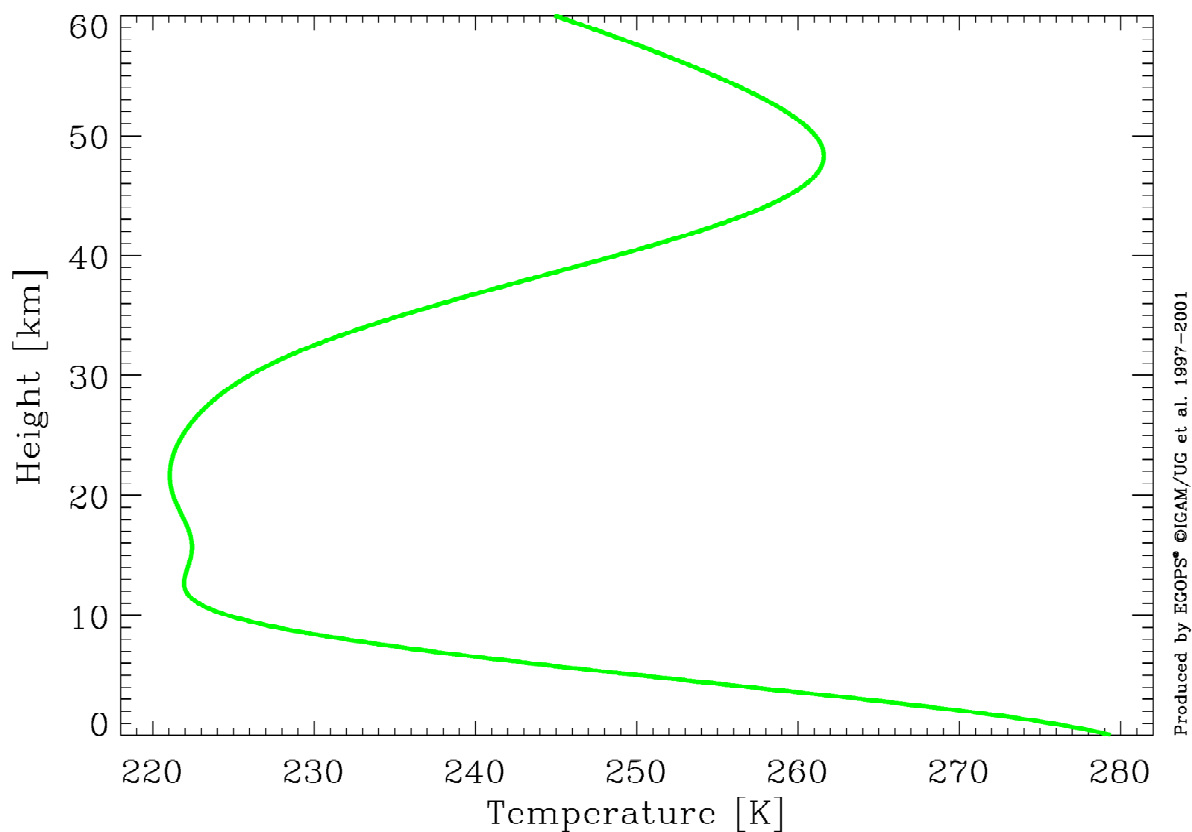
For this study, the almost finished EGOPS version 4 (finished in December 2001) was utilized as the basic tool. This basic version was then tailored and modified in a series of respects, as well as complemented by a few auxiliary software tools, in order to cope most effectively and conveniently with all functional and visualization requirements of the study.

3.2 Atmospheric models

Since the aim of the study is to describe the effects of the ionospheric conditions and the method of high-altitude initialization on the RO retrieval products, rather than effects of error sources internal to the neutral atmosphere, there was no need to use a highly sophisticated neutral atmosphere model. Quite contrary, it was important to supply the forward model with simple neutral atmosphere data in order to ensure that the errors in the subsequently retrieved atmospheric parameters would really be fully traceable to ionospheric residuals and the method of statistical optimization.

For the above reasons we used a dry atmosphere, artificially enforced local spherical symmetry to the neutral atmosphere, and used exactly the same conditions for all three simulated occultation events. The neutral atmosphere employed this way was the MSIS-90 model (Hedin, 1991) in the form tailored to EGOPS, in short MSIS model. We used the MSIS vertical profile data co-located with one of the selected occultation events (“nice” event, 63°N, 93°E, month: September, see section 4.3) for the forward modeling of all occultation events. Figure 3.1 displays the temperature profile at this location. The fact that the MSIS climatology was used also as a priori profile for statistical optimization (see section 2.2), adds some interesting aspects to the interpretation of the results (see section 4.1).

The ionosphere utilized in the forward modeling was the NeUoG model (Letinger and Kirchengast, 1997a; Hochegger *et al.*, 2000). This model was used in its full complexity (global 3D electron density distribution depending on local time, season, and solar activity) and features a high degree of asymmetrically distributed ionization (see section 3.4.2). The NeUoG model has already proven to be quite useful in several occultation-related studies (e.g., Letinger and Kirchengast, 1997b).



Temperature MSIS90 Location: Lat 63, Lon 93 [deg] Date: 99 09

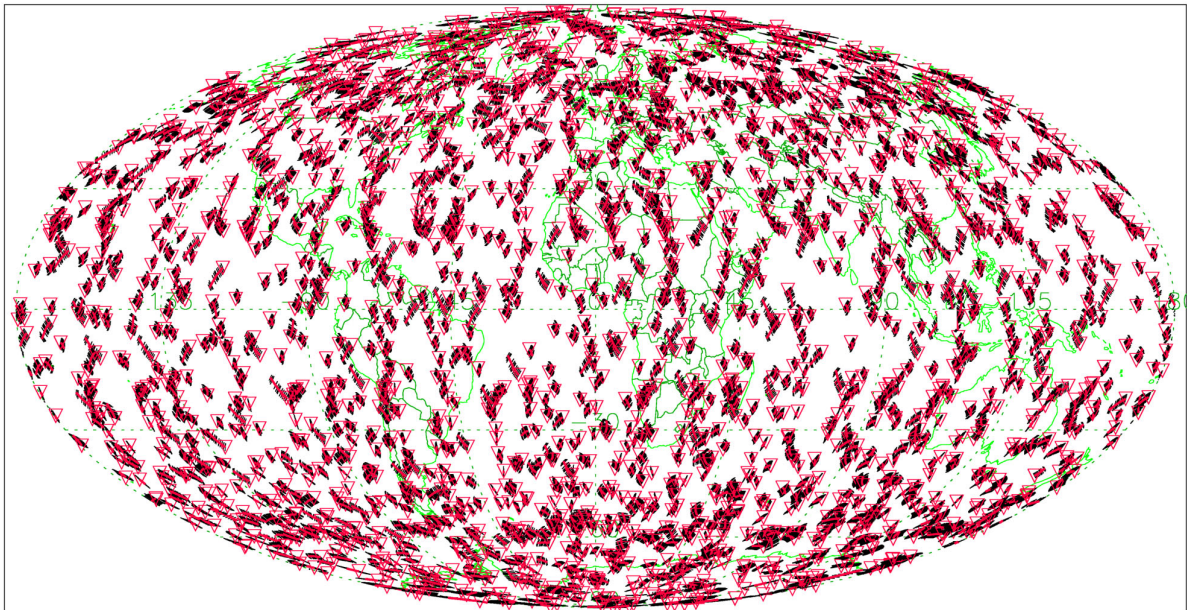
Figure 3.1: “True” temperature. The temperature profile was taken from the MSIS model (September, 63°N, 93°E). The corresponding model atmosphere (refractivity profile) was used for forward modeling of the occultation events.

3.3 Satellite mission simulation

The three representative occultation events were chosen from a one-day sample of a simulated satellite mission. For this purpose we constructed a constellation of 8 METOP-like satellites in two low Earth orbits (LEOs) flying at an altitude of 835 km. The two orbits were separated by 90°, the four satellites in each orbit were in-orbit-separated by 90° as well. Each simulated satellite carried a GNSS receiver. The GNSS transmitter constellation used in this study was the simulated realistic GPS system, consisting of the nominal 24 satellites.

For a 24 hour simulation period (September 15, 1999) the LEO-satellite constellation tracked ~2100 setting occultation events with a quite uniform global distribution. Figure 3.2 illustrates the coverage with events obtained. Rising occultation events were not included for convenience, as there is no specific need for doing so in this study focusing on stratospheric errors.

Occ. Event Distribution Data – Ground Projection Data



No.OccEv (∇ Setting,GPS): 2123 total, 2123/ 0 set/rise.
UT Range: 990915.000000,0240000

Figure 3.2: Modeled occultation events during 24 hrs on September 15, 1999.

3.4 The three representative occultation events

3.4.1 Geometrical properties

From the sample of ~2100 events we carefully chose three events according to the symmetry of the co-located ionosphere (see section 3.4.2). For the sake of simplicity we will hereafter refer to them as “nice”, “nasty 1”, and “nasty 2” event, respectively. The reason for this nomenclature will become clear in the next section.

The “nice” event is located over Central Siberia (63°N, 93°E) and its occultation plane is zonally oriented. The “nasty 1” and the “nasty 2” events are located over Oman (23°N, 56°E) and Albania (42°N, 19°E), respectively. The occultation planes of both “nasty” events are near-meridionally oriented. Figure 3.3 shows the location of the mean tangent points (triangles), the ground track of the tangent point trajectories (red lines, if color print, starting at the triangles), as well as the orientation of the rays (bundle of parallel lines) for the three representative occultation events.

Occ. Event Distribution Data – Ground Projection Data

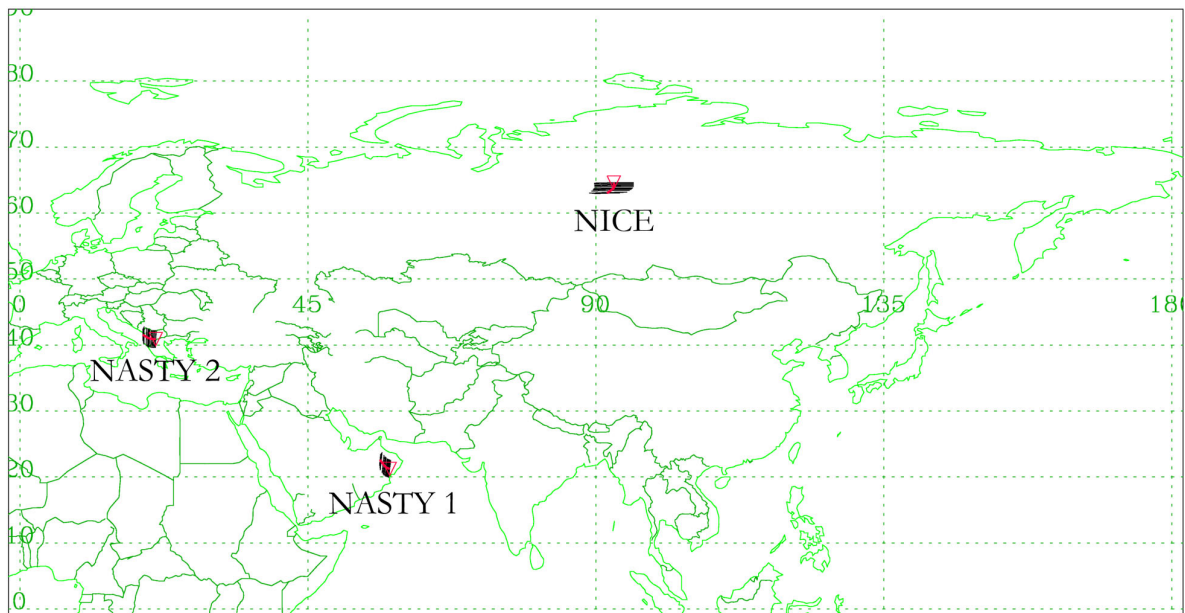


Figure 3.3: The three selected representative occultation events. The terms “nice” and “nasty” refer to the well (“nice”) or not so well behaved (“nasty”) symmetry of the co-located ionosphere.

3.4.2. Ionospheric conditions

The linear correction of bending angles involves the assumption of a spherically symmetric ionosphere. This is necessary to be able to define a proper impact parameter not varying along the ray path. Though there are no detailed studies under realistic conditions about this effect yet, asymmetries in the ionosphere are regarded to be a limiting error source for the retrieval of atmospheric parameters in the upper stratosphere and above (e.g., Kursinski *et al.*, 1997).

We selected three occultation events (all under daytime conditions, local time between 13:00 and 14:00 hrs), each of them being representative for one specific type of symmetry in the ionosphere. The events and the prevailing ionospheric conditions are illustrated in Figures 3.4 to 3.6: The upper panels show the global maps of the vertical total electron content and the locations of the mean tangent points (black crosses). Furthermore, the orientation of the occultation rays is symbolized by black lines. The lower panels show vertical sections through the atmosphere at the latitude (nice event) or the longitudes (nasty 1 and nasty 2 events) of the occultation planes. The white curved lines illustrate the lowermost ray path of the respective occultation event.

The “nice” event (Figure 3.4) was chosen to be zonally oriented, since the electron density gradients are much lower in this direction. Therefore, and due to careful selection of the occultation event’s location, the spherical symmetry assumption is met as good as it is possible in a realistic ionosphere during daytime conditions. The two “nasty” events (Figures 3.4 and 3.5) were chosen to be meridionally oriented for complementary reasons. In these two cases we tried to find situations that violate the spherical symmetry assumption in a particular severe manner. There are two different types of asymmetry: The first one (nasty 1, Figure 3.5) exhibits relatively low electron densities at the in- and outbound of the ray and a maximum in electron density above the perigee of the occultation. This will be a challenging case for advanced ionospheric correction schemes trying to exploit the ionosphere profile information

available above the neutral atmosphere profile. The second one (nasty 2, Figure 3.6) exhibits low electron densities at the inbound and high electron densities at the outbound of the ray.

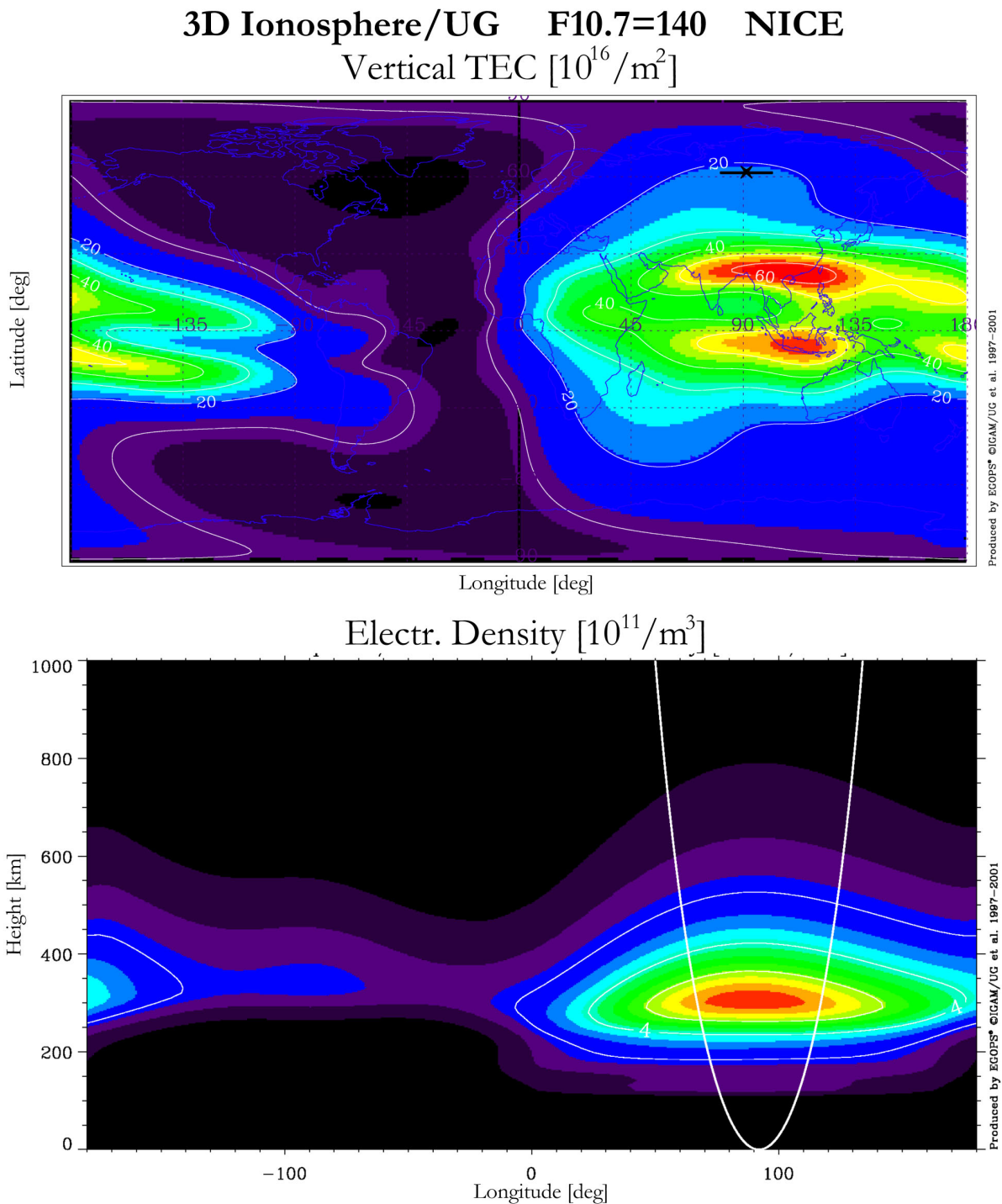


Figure 3.4: Ionospheric conditions during the “nice” occultation event. Vertical total electron content above the mean tangent point: $\sim 20 \cdot 10^{16} \text{ m}^{-2}$. The electron density varies less than $1.5 \cdot 10^{11} \text{ m}^{-3}$ between inbound and outbound of the lowermost occultation ray.

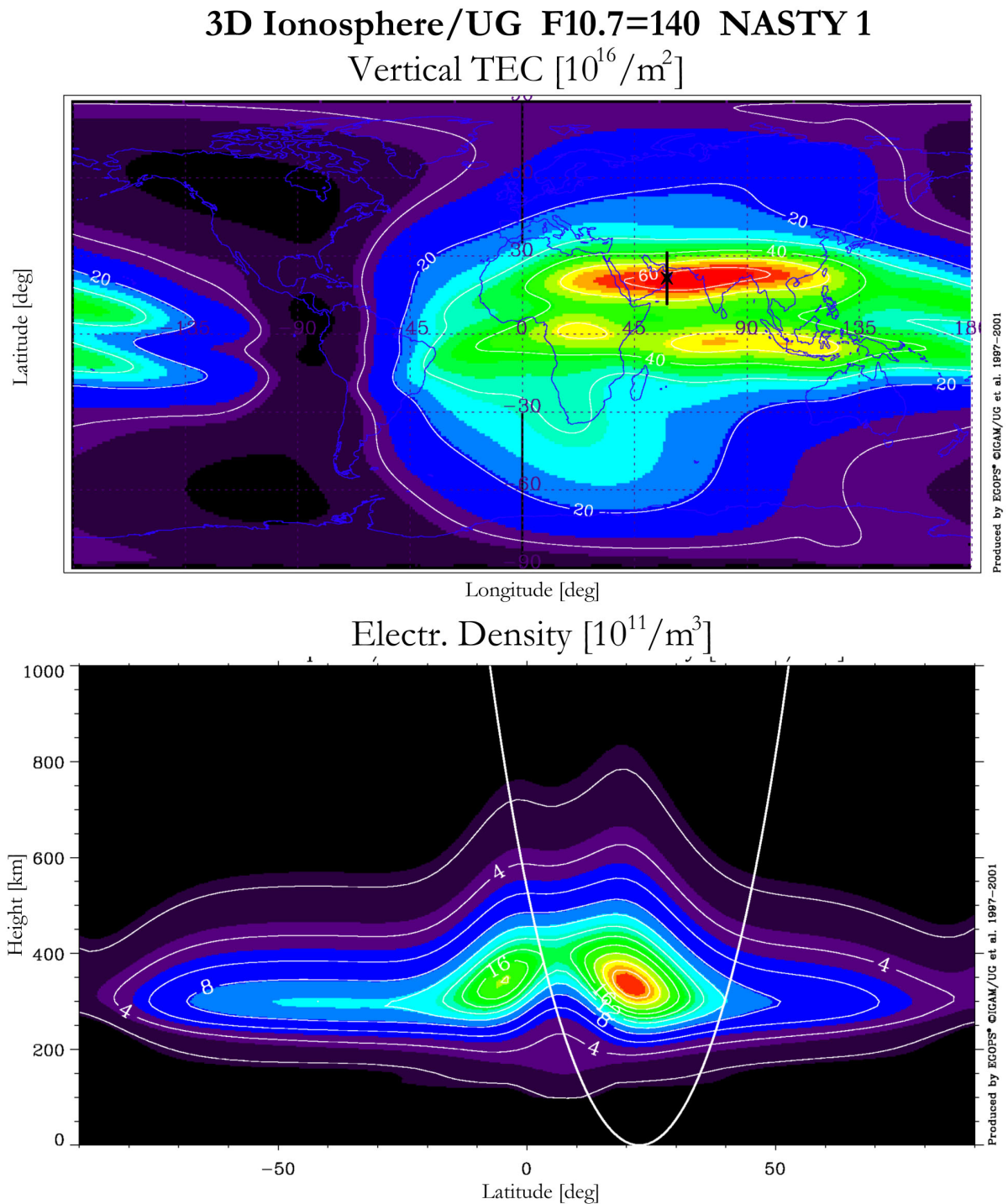
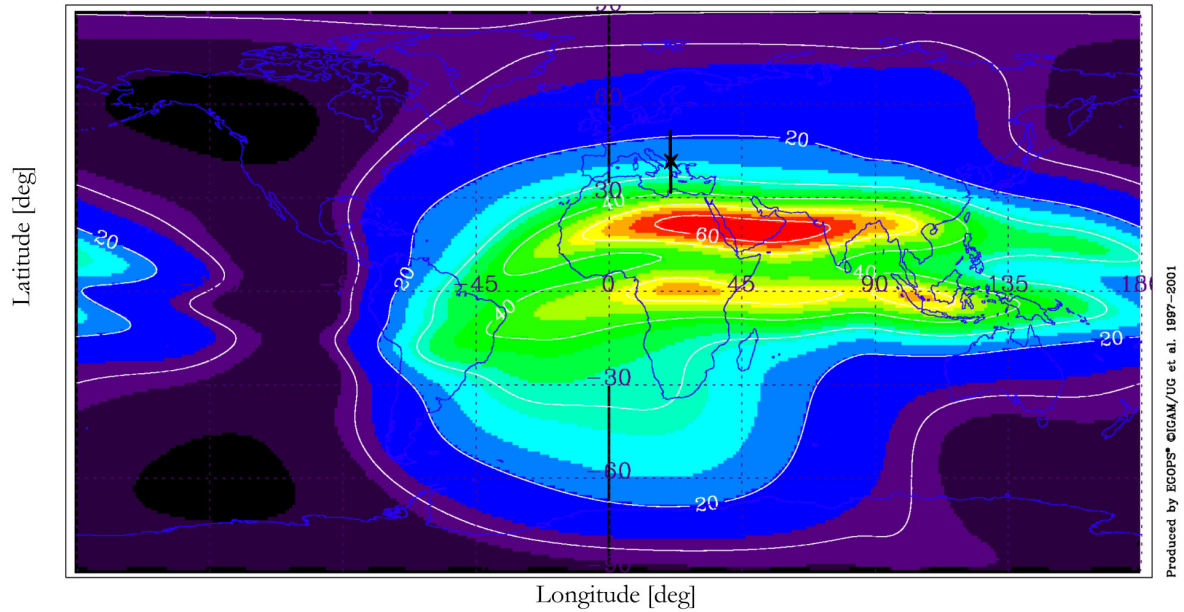


Figure 3.5: Ionospheric conditions during the “nasty 1” occultation event. Vertical total electron content above the mean tangent point: $\sim 60 \cdot 10^{16} \text{ m}^{-2}$. The electron density varies up to $12 \cdot 10^{11} \text{ m}^{-3}$ between inbound and outbound of the lowermost occultation ray. The maximum electron density is located directly above the neutral atmosphere tangent point location of the occultation.

3D Ionosphere/UG F10.7=140 NASTY 2

Vertical TEC [$10^{16}/\text{m}^2$]



Electr. Density [$10^{11}/\text{m}^3$]

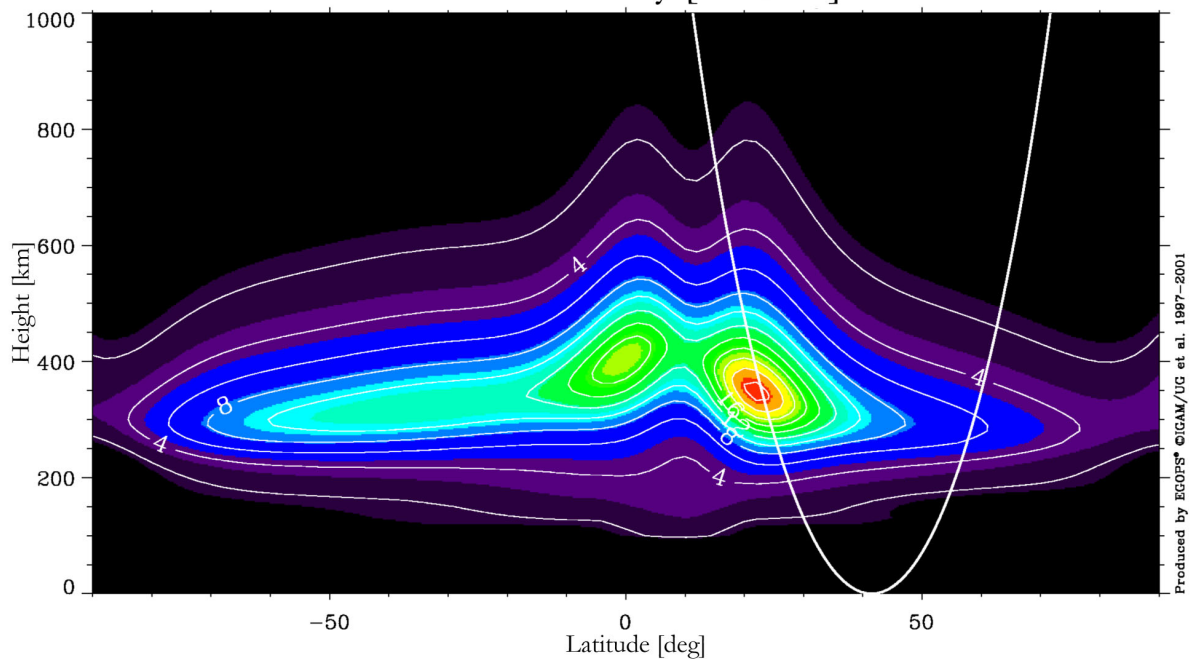


Figure 3.6: Ionospheric conditions during the “nasty 2” occultation event. Vertical total electron content above the mean tangent point: $\sim 25 \cdot 10^{16} \text{ m}^{-2}$. The electron density varies up to $18 \cdot 10^{11} \text{ m}^{-3}$ between inbound and outbound of the lowermost occultation ray. The maximum electron density is found at the outbound of the lowermost ray.

4. Results

In this section we present and discuss selected retrieval results. For demonstration purposes we mainly use the error of the observed temperature. Both the retrieval results for data from a realistic receiving system as well as from an idealized receiving system are presented (cf. section 3). A comprehensive survey of all retrieved parameters investigated (bending angle, refractivity, pressure, geopotential height, and temperature) is given in Appendix A for the realistic receiving system and in Appendix B for the ideal receiving system.

Each representative occultation (nice, nasty 1, and nasty 2; introduced in section 3.4) was simulated for four ionization levels as explained in section 3. Each single error profile in one row of the following figures – starting with Figure 4.3 – corresponds to the same ionization level, indicated by the $F_{10.7}$ value or the note “No Ion.” at the left-hand side of the row. The retrieval of each simulated occultation event was performed using three different types of statistical optimization as explained in section 2.2. Each single error profile in one column of the following figures corresponds to the same statistical optimization approach. Except for Figure 4.5 the left-hand column corresponds to no optimization (exponential extrapolation), the middle column to heuristic optimization (co-located a priori profile from MSIS), and the right-hand column to inverse covariance weighting optimization (best-fit a priori profile from global search in MSIS model domain), respectively.

On top of each individual error profile panel two measures of quality referring to the average error estimate in the 35 to 45 km height interval are given: The bias, which describes the mean deviation of the retrieved profile from the “true” profile in this interval, and the standard deviation (stddev), which describes the mean fluctuation of the bias-corrected retrieved profile in the same interval. To show an instructive example of these quality measures, we illustrate the bias and standard deviation values associated with the retrieved temperature profiles in Figures 4.1 and 4.2. The values for all computed scenarios are displayed, for both the no-optimization retrieval scheme and the inverse covariance weighting retrieval scheme, respectively. We will refer to Figures 4.1 and 4.2 several times in the discussion below.

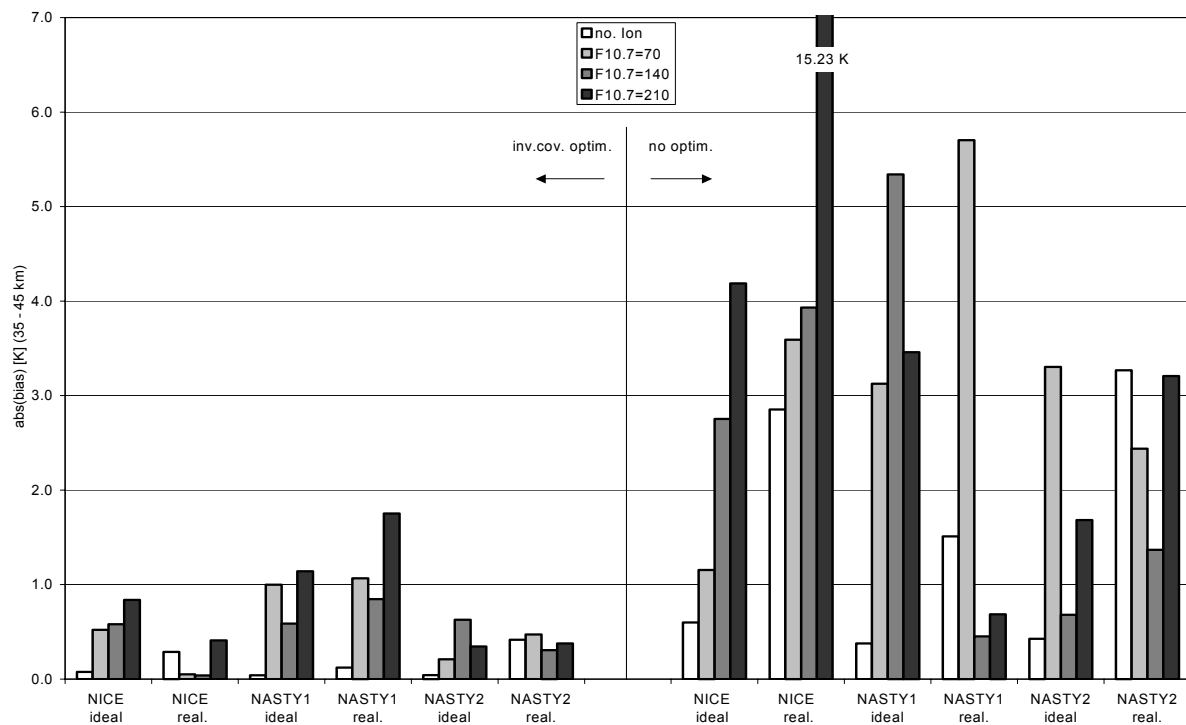


Figure 4.1: Bias of the retrieved temperature in the 35 to 45 km interval for all simulated occultation events at different ionospheric conditions and with different simulated receiving systems (ideal and quasi-realistic receiving system). Left: retrieval with inverse covariance weighting optimization. Right: retrieval with no optimization.

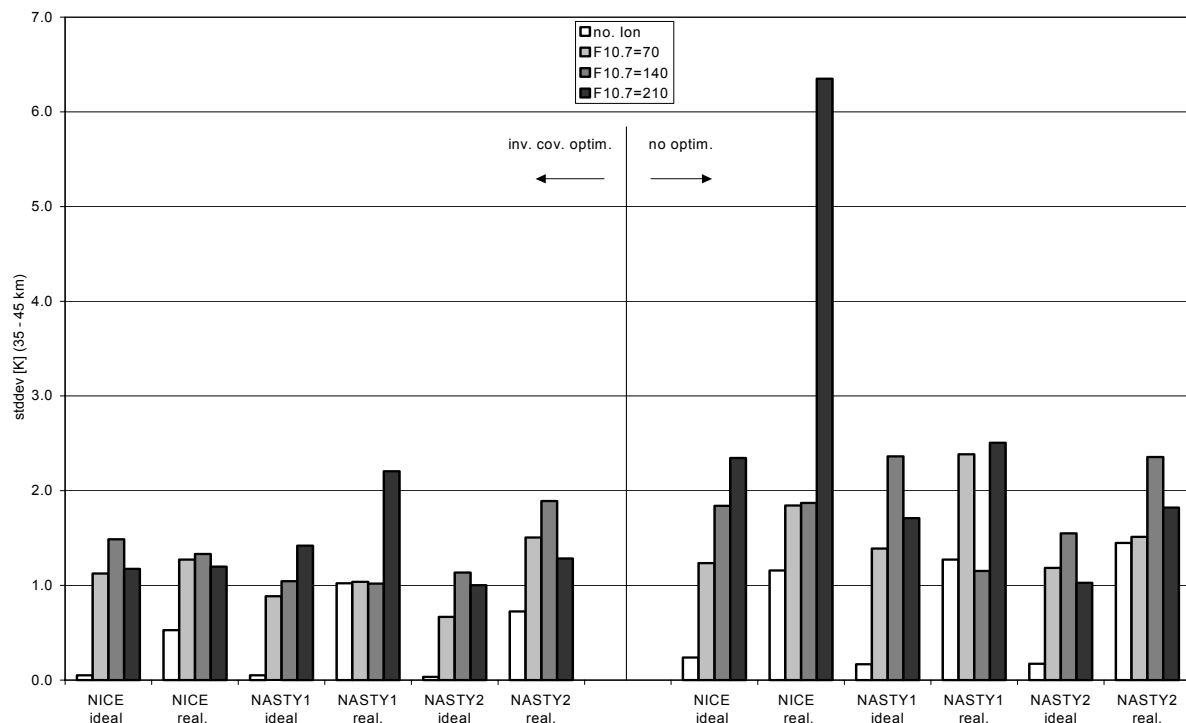


Figure 4.2: Standard deviation of the retrieved temperature in the 35 to 45 km interval for all simulated occultation events at different ionospheric conditions and with different simulated receiving systems (ideal and quasi-realistic receiving system). Left: retrieval with inverse covariance weighting optimization. Right: retrieval with no optimization.

4.1 The effects of statistical optimization

The principal effect of statistical optimization can best be demonstrated using idealized conditions. Figure 4.3 shows the retrieved temperature error profiles with ionosphere “switched off” and ideal receiving system for the “nice” event. Without statistical optimization the measurements becomes biased towards higher temperatures at heights above 35 km. The direction and magnitude of the bias is highly influenced by the selection of the initial height used in the retrieval (see also to the left rows of Figures 4.7 to 4.8). This is due to the fact that above ~50 km, where the exponential profile is fitted to the observed bending angle profile, the signal-to-noise ratio becomes low and small changes in the initial height can correspond to large differences in the observed bending angle values (e.g., Rieder and Kirchengast, 2001).

Applying statistical optimization, we get significantly better results: The bias remains below 1 K up to 60 km for both statistical optimization approaches. In this case (“nice” occultation event) it makes no difference whether we perform a priori profile search or not, since the neutral atmosphere conditions used in the forward model are the same as in the a priori data. In other words, even without a priori search, we automatically use the optimal a priori profile in this case. The two optimization approaches yield more or less similar results. Figure 4.6 in section 4.2, which again shows the temperature retrieval error for the “nice” event (for a more realistic scenario), indicates that inverse covariance weighting optimization is superior to heuristic optimization at high altitudes (above 50 km). As long as a priori profile search is not relevant (i.e., as long as the a priori profile is unbiased), the effect is small compared to other error sources, however.

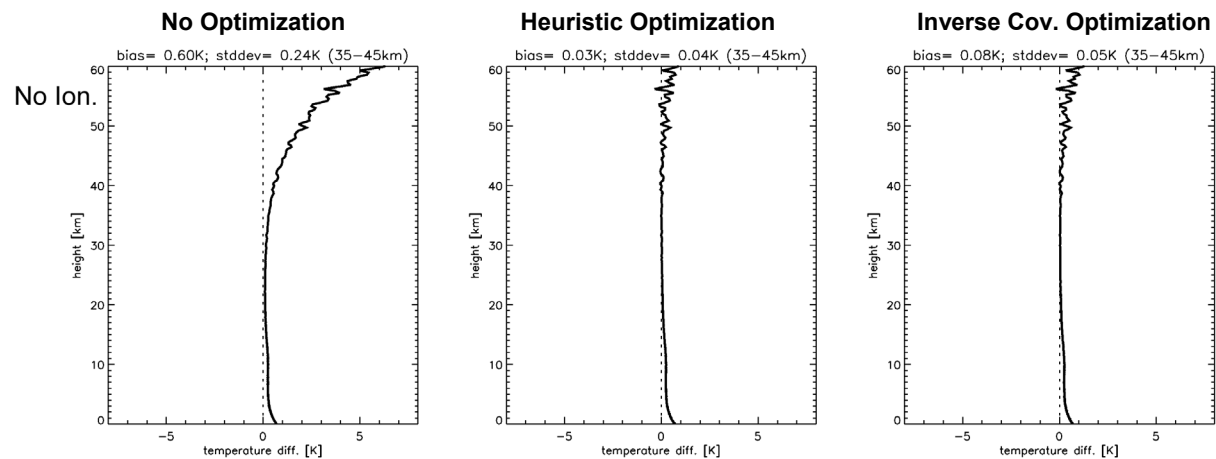


Figure 4.3: Temperature retrieval error (nice event) for no ionosphere/ideal receiving system.

In Figures 4.1 and 4.2, the upper-stratosphere temperature errors of the no-optimization retrieval and the inverse covariance weighting retrieval of all occultation events (nice, nasty 1 and nasty 2, each with ideal and realistic receiving system) at all modeled ionization levels can be compared. Figure 4.1 clearly shows that statistical optimization strongly reduces the temperature bias between 35 and 45 km in almost every case. On average, the bias is reduced to about one-third (more precisely, 36%) of the no-optimization bias in this ensemble of cases. In addition, there is a smaller but also significant improvement in the standard

deviation (Figure 4.2): it is reduced, on average, to about two-third (more precisely, 66%) of the no-optimization standard deviation.

In Figure 4.4 the temperature error profiles for the same scenario as in Figure 4.3 (no ionosphere, ideal receiver) but for the “nasty 2” event is shown. Since this occultation event was simulated with the same atmospheric properties as the “nice” event in Figure 4.3, the retrieval results should be the same. The bias of the no-optimization case resembles the bias in Figure 4.3, but is slightly smaller. As the only difference between both scenarios is the location of the events, this can only be due to geometrical reasons. In addition, there are some small differences in the troposphere and lower stratosphere (see section 4.4).

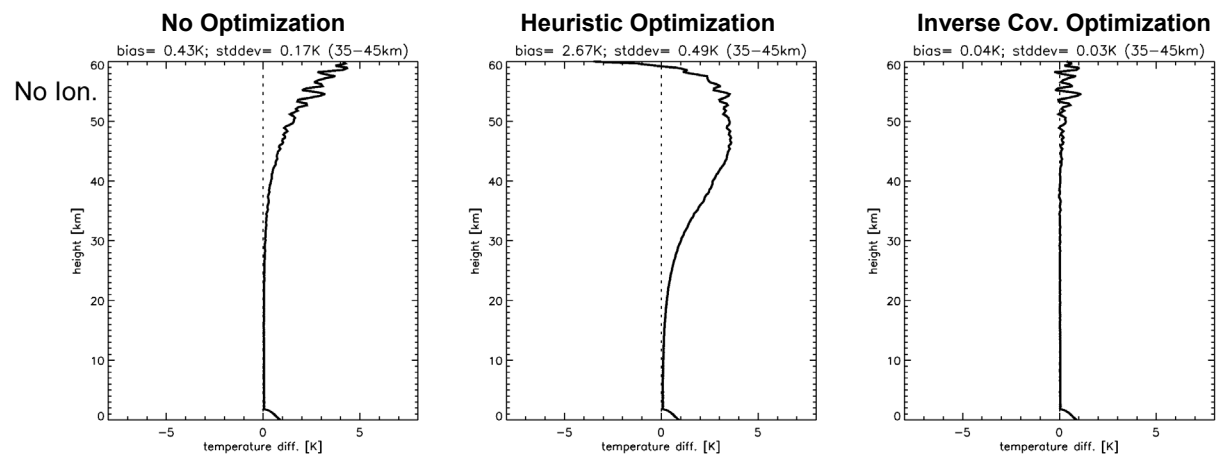


Figure 4.4: Temperature retrieval error (nasty 2 event) for no ionosphere/ideal receiving system.

The discrepancy between the two different statistical optimization approaches shown in Figure 4.4 exemplify the importance of good quality a priori data: The heuristic optimization simply uses the co-located profile from climatology as a priori profile, which is (a priori) wrong in this case. Though the error of the a priori profile used here, compared to the optimal a priori profile used in Figure 4.3, is $< 8\%$ in the stratosphere and mesosphere (clearly within the assumed uncertainty of 20%; see section 2.2), the effect is a marked degradation of retrieval performance in the upper stratosphere, even compared to the no-optimization case. The inverse covariance weighting approach with search, on the other hand, manages to find a good a priori profile and provides a temperature retrieval of the same quality as in Figure 4.3.

It is important to note that the superiority of the latter approach is not only achieved due to its superior theoretical-statistical foundation (account for error correlations, more adequate observation error definition; cf. Healy, 2001) but also due to the a priori profile search algorithm involved. This is illustrated in Figure 4.5, showing a comparison of the heuristic approach (left panel) and the inverse covariance weighting approach without (middle panel) and with a priori profile search (right panel), respectively, for one exemplary scenario (nasty 1 event, $F_{10.7} = 70$, realistic receiving system). The inverse covariance optimization without search does significantly enhance the retrieval as compared to the heuristic approach, but the temperature still exhibits a marked bias in the upper stratosphere (2.35 K within 35-45 km in the **typical** example shown). Including the search for an optimal a priori profile leads to a significant further reduction of this upper stratospheric bias to ~ 1 K.

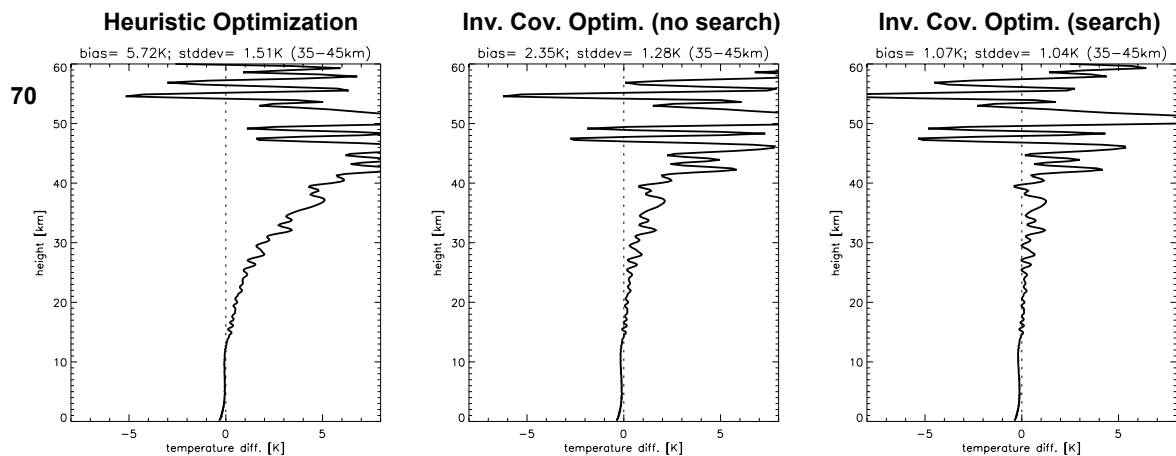


Figure 4.5: Temperature retrieval error (nasty 1 event) for $F_{10.7} = 70$ ionization level/realistic receiving system.

4.2 The effects of ionization level and ionospheric symmetry

Figures 4.6 to 4.8 show more realistic scenarios: We included the NeUoG ionosphere in the forward modeling process and simulated a realistic (GRAS-like) receiving system.

Figure 4.6 shows the error of the temperature retrieval of the occultation event with almost spherically symmetric electron density distribution (nice event). In this case rising ionization levels significantly downgrade the no-optimization retrieval performance. This can also be clearly seen in the bias and standard deviation values in Figures 4.1 and 4.2, respectively (nice event cases of the no-optimization part). Statistical optimization largely compensates for this ionization-level dependence (nice event cases of the inverse covariance optimization part).

As illustrated in Figures 4.7 and 4.8, the situation is not that clear for the two asymmetric ionosphere events (nasty 1 and nasty 2). Interestingly, it can not be concluded that rising ionization levels necessarily lead to a corresponding degradation of retrieval products, a somewhat counter-intuitive evidence also clearly visible in Figures 4.1 and 4.2 (see, e.g., nasty 1 and nasty 2 event cases of the no optimization part).

Similarly, if we compare the three different representative occultation events with each other – each reflecting a distinctly different ionospheric a/symmetry setting – we see no clear evidence for degraded retrieval results under asymmetric conditions, compared to symmetric conditions, in the ionosphere (see also Figures 4.1 and 4.2). Interestingly again, we thus can not conclude from these results that highly asymmetric ionospheric conditions have a strong negative effect on RO retrieval performance. This indicates that the linear correction of bending angles seems, favorably, not very vulnerable to the violation of the spherical symmetry assumption intrinsic in its impact parameter formulation.

Just as demonstrated in section 4.1 by an idealized example, the retrieval of the quasi-realistic occultation events with heuristic statistical optimization produces good results only as long as it is assured that the a priori profile matches the actual atmospheric conditions at the event location (compare Figures 4.7 and 4.8, where a “wrong” a priori profile is used). The inverse covariance weighting approach with a priori profile search enhances the quality of the retrievals in almost any case.

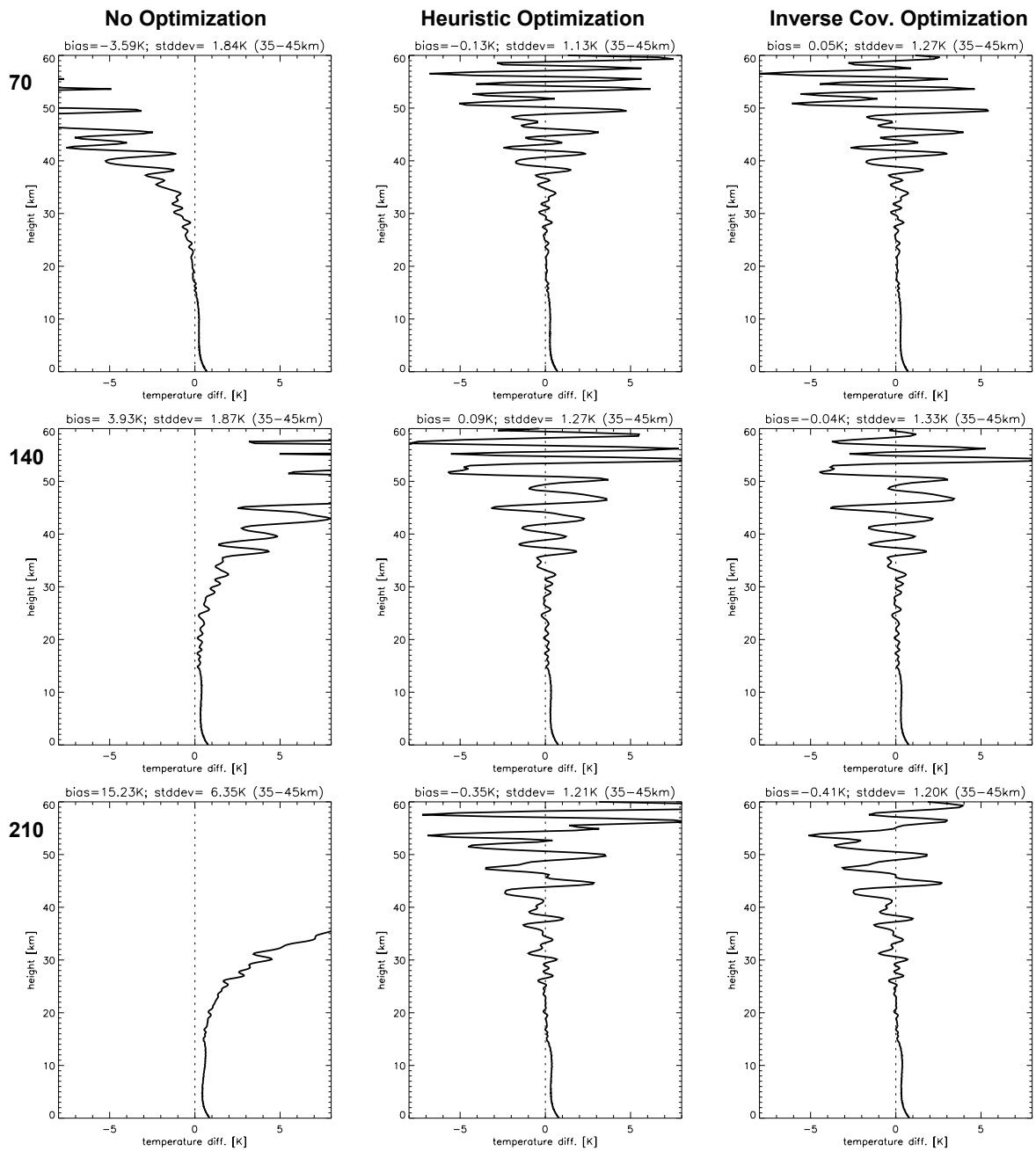


Figure 4.6: Temperature retrieval error (nice event) for different ionization levels ($F_{10.7}=70$, $F_{10.7}=140$, $F_{10.7}=210$) and realistic (GRAS-like) receiving system.

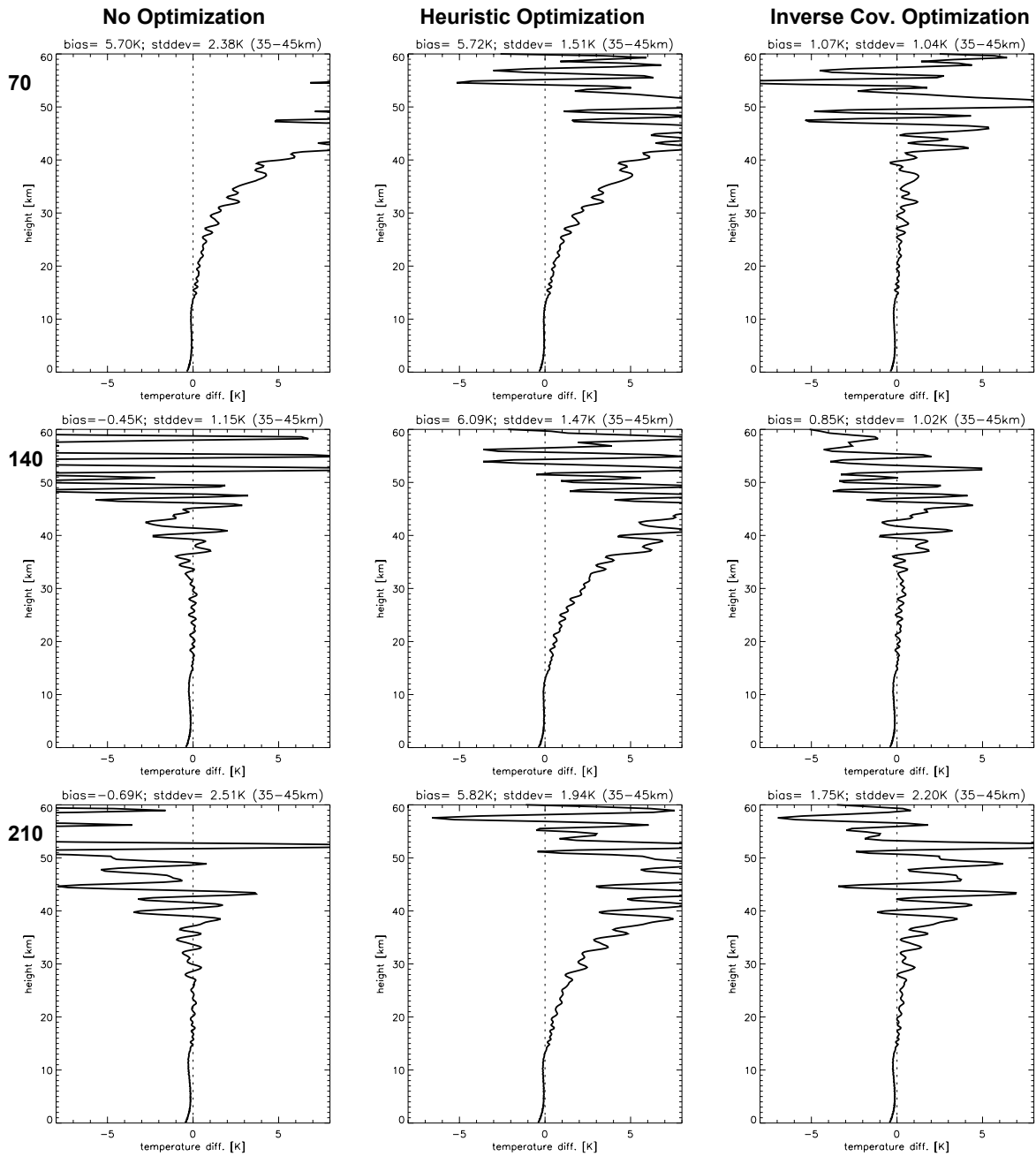


Figure 4.7: Temperature retrieval error (nasty 1 event) for different ionization levels ($F_{10.7} = 70$, $F_{10.7} = 140$, $F_{10.7} = 210$) and realistic (GRAS-like) receiving system.

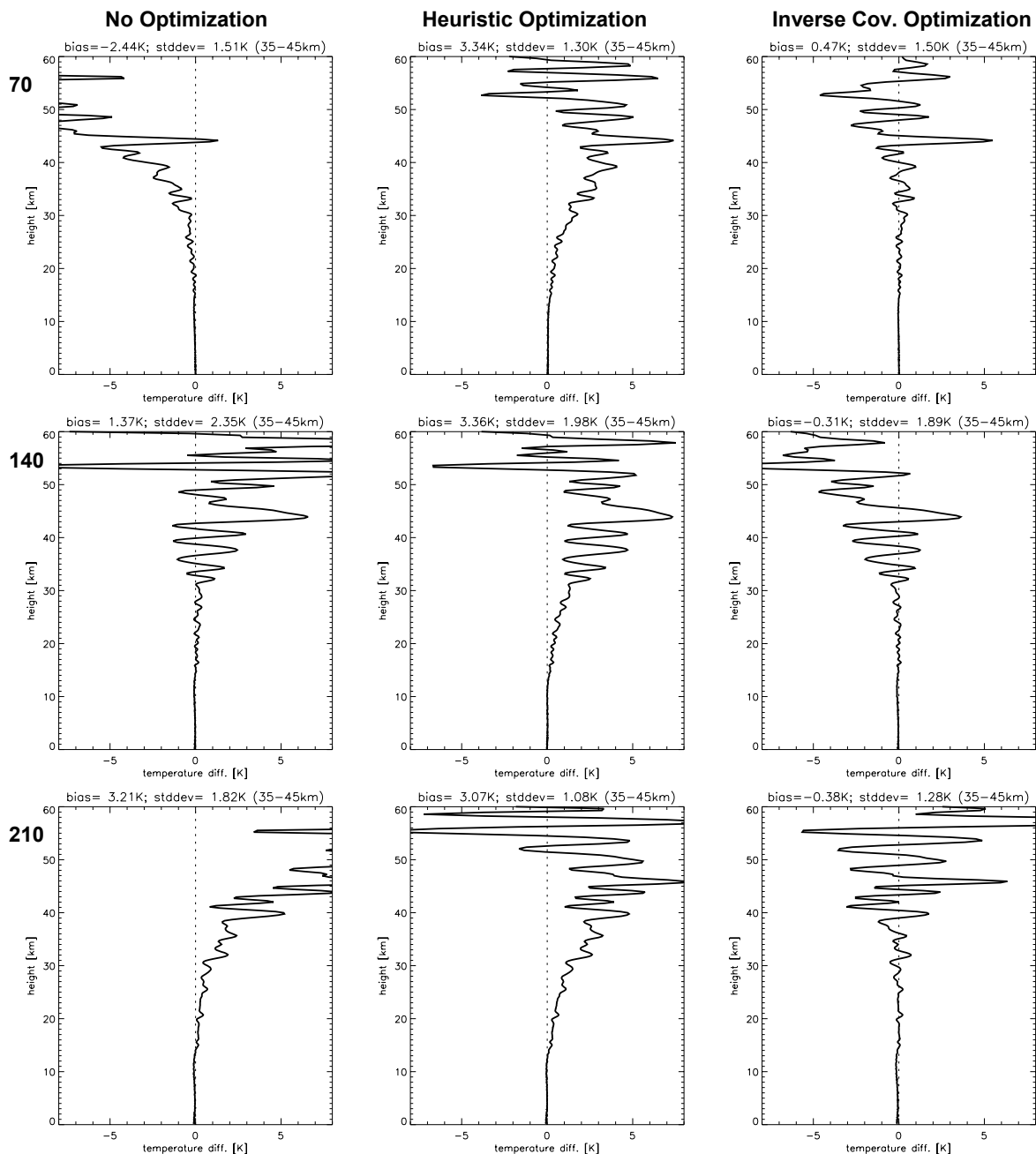


Figure 4.8: Temperature retrieval error (nasty 2 event) for different ionization levels ($F_{10.7} = 70$, $F_{10.7} = 140$, $F_{10.7} = 210$) and realistic (GRAS-like) receiving system.

4.3 Interaction between ionospheric residuals and statistical optimization

As the results of this study have shown, the a priori profile search prior to statistical optimization increases the value of statistical optimization in a substantial way. If the ionospheric correction leaves a very significant residual, the a priori profile search can be misguided, though, since it searches for pure neutral atmosphere bending angle profiles. Usually the retrieval is still improved in such cases, but in some extreme cases the retrieval products get degraded. We can detect such a situation in Figure 4.7 (nasty 1 event) at high ionization level ($F_{10.7} = 210$). It is visible in this case that the inverse covariance weighting

approach leads to a temperature profile in the upper stratosphere, which is inferior to the no-optimization approach. Currently we believe to understand the principal mechanism leading to this effect (as explained above), but in-depth understanding is necessary to be able to avoid it. It seems worthwhile in this context to explore in future work the interaction between statistical optimization and ionospheric correction in more detail.

4.4 Residuals in the troposphere and lower stratosphere

In the lower part of the temperature error profiles (e.g., Figures 4.6 to 4.8) each representative occultation event features a characteristic small-residual-error pattern which is independent of the retrieval method and the level of ionization. These patterns appear even in the no-ionosphere cases (e.g., Figures 4.3 and 4.4), thus they are not correlated to the a/symmetry of the electron density distribution as well. As we explicitly excluded horizontal variability in the neutral atmosphere, it is also not related to deviations from spherical symmetry in the troposphere.

We did not investigate this small residual error in further detail here, as it is not relevant within the focus of this study (ionospheric correction and high-altitude initialization). Preliminary separate evidence obtained so far indicates, though, that it is a systematic error (bias), that it is not related to the correction for the Earth’s oblateness (Syndergaard, 1998), and that it may come in due to some tiny inaccuracy in the treatment of occultation event geometry. Since the bias is observed to be able to reach a few 0.1 Ks, including in the lower stratosphere, we consider its mitigation important for ensuring optimal climate monitoring utility of RO measurements. Future work will thus be performed to eliminate this residual.

5. Conclusion and Outlook

This systematic case-study was designed to investigate the sensitivity of atmospheric profiles retrieved from GNSS radio occultation data to ionospheric residual errors and high-altitude initialization errors.

Two processes need to be applied to ensure good retrieval performance: ionospheric correction techniques to minimize the ionosphere-induced errors and statistical optimization techniques to smooth noisy observed data by less noisy a priori data. Both methods are vital and important to minimize high-altitude errors and, in particular, the propagation of such errors downward into the stratosphere.

We simulated various different ionospheric situations to elaborate the potential residuals of ionospheric correction by linear combination of bending angles. In addition, we applied three different methods of statistical optimization: classical exponential extrapolation of bending angles, heuristic statistical optimization, and inverse covariance weighted optimization with a priori-profile search, respectively.

The results confirm results from previous studies that the classical exponential extrapolation of bending angle profiles (“no optimization”) can be significantly enhanced by combining the observed atmospheric profile with data from climatological models (i.e., by supplying a priori information), either by heuristic optimization or by inverse covariance weighting optimization.

The results reveal that the quality of the selected a priori profile plays a crucial role for the performance achieved; even if the error of the a priori profile is smaller than the statistical uncertainty assumed in the heuristic optimization algorithm, statistical optimization can severely degrade the retrieval accuracy. In order to avoid this effect, a search algorithm providing a best-fit climatological a priori profile is highly useful. This algorithm, if employed prior to and combined with the inverse covariance weighting optimization method, yielded the best results. Nevertheless, while this advanced algorithm is generally much less vulnerable to residuals from ionosphere correction than classical exponential extrapolation, we found one high-ionization case where the latter performed better.

Furthermore, the results indicate that the applied linear ionosphere correction of bending angles is remarkably robust against the violation of the ionospheric spherical symmetry assumption intrinsic in its impact parameter formulation. We found no convincing evidence for both, highly asymmetric ionospheric conditions and high ionization levels, that these do systematically degrade the RO retrieval performance if the inverse covariance weighting optimization with prior a priori profile search is applied.

Concerning further improvements to the quality of upper stratospheric RO retrieval products, it seems to be most promising to pay more attention to improved error characteristics of a priori data (i.e., to prepare profile libraries superior to MSIS climatology and/or to exploit suitable short-range forecast profiles) as well as to optimize methods of fitting the a priori data to the atmospheric conditions as expressed by the observed data. More generally, it is worth to explore the relative merits of the bending angle optimization approach and applications of the more general optimization approach suggested by Rieder and Kirchengast (2001).

A related topic worth future investigation is, under which (extreme) ionospheric conditions the background search may be misled by residual ionospheric errors, a matter touching the interesting question of interaction between ionospheric correction and statistical optimization. These investigations will also provide evidence on the degree to which further (higher-order) ionospheric correction scheme developments are required even when advanced statistical optimization schemes (optimized as outlined in the previous paragraph) are available.

As a spin-off result of the study, re-enforcing indications from other recent error analysis work at IGAM, evidence was found for small residual biases in the troposphere and lower stratosphere in some geographical regions. These may be related to some residual inaccuracy in the treatment of occultation event geometry. Further investigation and mitigation of these biases will be performed in the future in order to ensure optimal climate monitoring utility of GNSS RO measurements.

Acknowledgments. The EGOPS software, the core tool of the study, was developed by an international consortium led by IGAM/UG and involving partner teams at Danish Meteorological Institute and TERMA Elektronik A/S, Denmark, the Met. Office, U.K., and Austrian Aerospace GmbH, Austria, with the major funding provided by the European Space Agency. The European Centre for Medium-Range Weather Forecasts (ECMWF, Reading, U.K.) provided the atmospheric analysis field used. The study was funded by the European Space Agency under ESA/ESTEC Contract No. 14809/00/NL/MM. Furthermore, A.G. received financial support for the work from the START research award of G.K. funded by the Austrian Ministry for Education, Science, and Culture and managed under Program No. Y103-CHE of the Austrian Science Fund.

References

- Gorbunov, M.E., A.S. Gurvich, and L. Bengtsson**, Advanced algorithms of inversion of GPS/MET satellite data and their application to reconstruction of temperature and humidity, *Rep. No. 211*, Max-Planck-Institut für Meteorologie, Hamburg, Germany, 1996.
- Gorbunov, M.E., and A.S. Gurvich**, Algorithms of inversion of Microlab-1 satellite data including the effects of multipath propagation, *Int. J. Remote Sensing*, 19, 12, 2283-2300, 1998.
- GRAS-SAG**, The GRAS instrument on METOP, *ESA/EUMETSAT Rep. (ESA No. VR/3021/PI, EUM.No. EPS/MIS/IN/9)*, 38 pp., ESA/ESTEC, Noordwijk, Netherlands, 1998.
- Healy, S.B.**, Smoothing radio occultation bending angles above 40 km, *Ann. Geophysicae*, 19, 495-468, 2001.
- Hedin, A.E.**, Extension of the MSIS thermosphere model into the middle and lower atmosphere, *J. Geophys. Res.*, 96, 1159-1172, 1991.
- Hoegger, G., B. Nava, S. Radicella, and R. Leitinger**, A family of ionospheric models for different uses, *Phys. Chem. Earth (C)*, 25, 4, 307-310, 2000.
- Hocke, H., G. Kirchengast, A. Steiner**, Ionospheric correction and inversion of GNSS occultation data: problems and solutions, *IMG/UoG Tech. Rep. For ESA/ESTEC No. 2/97*, Inst. of Meteorol. and Geophys., Univ. of Graz, Austria, 1997.
- Hocke, K.**, Inversion of GPS meteorology data, *Ann. Geophysicae*, 15, 443-450, 1997.
- Hoeg, P., A.S. Jensen, H. Vedel, E. Kaas, and G. Kirchengast**, ACE (Atmosphere Climate Experiment) Scientific Support Study, *Proposal to ESA/ESTEC*, 40p., Danish Met. Institute, Copenhagen, Denmark, 2000.
- Kirchengast, G.**, End-to-end GNSS Occultation Performance Simulator overview and exemplary applications, *Wissenschaftl. Ber. No. 2/1998*, Inst. for Meteorol. and Geophys., Univ. of Graz, Austria, 1998.
- Kirchengast, G., J. Fritzer, and J. Ramsauer**, End-to-end GNSS Occultation Performance Simulator Version 4 (EGOPS4) Software User Manual (Overview and Reference Manual), *Techn. Report for ESA/ESTEC No. 5/2001*, Inst. for Geophys., Astrophys., and Meteorol., Univ. of Graz, Austria, 2001.
- Kursinski, E.R., G.A. Hajj, J.T. Schofield, R.P. Linfield, and K.R. Hardy**, Observing earth's atmosphere with radio occultation measurements using the Global Positioning System, *J. Geophys. Res.*, 102, D19, 23429 - 23465, 1997.
- Ladreiter, H.P., and G. Kirchengast**, GPS/GLONASS-sensing of the neutral atmosphere: Model independent correction of ionospheric influences, *Radio Sci.*, 31, 877-891, 1996.
- Leitinger, R., and G. Kirchengast**, Easy to use global and regional models - a report on approaches used in Graz, *Acta Geod. Geophys. Hung.*, 32, 329-342, 1997a.
- Leitinger, R., and G. Kirchengast**, Inversion of the plasma signal in GNSS occultations - simulation studies and sample results, *Acta Geod. Geophys. Hung.*, 32, 379-394, 1997b.
- Melbourne, W.G., E.S. Davies, C.B. Duncan, G.A. Hajj, K.R. Hardy, E.R. Kursinski, T.K. Meehan, L.E. Young**, The application of spaceborne GPS to atmospheric limb

- sounding and global change monitoring, *JPL Publication 94-18*, Jet Propulsion Laboratory, California Institute of Technology, Pasadena, California, 1994.
- Rieder, M.J., and G. Kirchengast**, Error analysis and characterization of atmospheric profiles retrieved from GNSS occultation data, *J. Geophys. Res.*, 106, 31,755-31,770, 2001.
- Rodgers, C. D.**, Retrieval of atmospheric temperature and composition from remote measurements of thermal radiation, *Rev. Geophys. Space Phys.*, 14, 609-624, 1976.
- Rodgers, C. D.**, Characterization and error analysis of profiles retrieved from remote sounding measurements, *J. Geophys. Res.*, 95, 5587-5595, 1990.
- Rodgers, C. D.**, *Inverse Methods for Atmospheric Sounding: Theory and Practice*, 256 pp., World Scientific Publ., Singapore, 2000.
- Sokolovskiy, S., and D. Hunt**, Statistical optimization approach for GPS/Met data inversions, URSI GPS/Met Workshop, Tucson, Arizona, 1996.
- Spilker, J.J., Jr.**, GPS signal structure and performance characteristics, in *Global Positioning System, Vol. 1*, 29-54, 1980.
- Steiner, A.K., G. Kirchengast, and H.P. Ladreiter**, Inversion, error analysis and validation of GPS/MET occultation data, *Ann. Geophysicae*, 17, 122-138, 1999.
- Steiner, A.K., G. Kirchengast, U. Foelsche, L. Kornblueh, E. Manzini, and L. Bengtsson**, GNSS occultation sounding for climate monitoring, *Phys. Chem. Earth (A)*, 26, 113–124, 2001.
- Syndergaard, S.**, On the ionosphere calibration in GPS radio occultation measurements, *Radio Sci.*, 35, 3, 865-883, 2000.
- Syndergaard, S.**, Modeling the impact of the Earth’s oblateness on the retrieval of temperature and pressure profiles from limb sounding, *J. Atmos. Solar-Terr. Phys.*, 60, 171-180, 1998.
- Vorob’ev, V.V., and T.G. Krasnil’nikova**, Estimation of the accuracy of the atmospheric refractive index recovery from Doppler shift measurements at frequencies used in the NAVSTAR system, *Phsy. Atmos. Ocean*, 29, 602-609, 1994.

(page intentionally left blank; back-page if double-sided print)

Appendix A. Retrieval Results – Realistic Receiving System

In Appendices A and B we present a comprehensive compilation of the ACCESS WP3200 study results. Appendix A shows the results for a quasi-realistic (METOP/GRAS-like) receiving system including all observation system-related error sources such as orbit uncertainties, receiver noise, local multipath errors and clock errors. Appendix B shows the results for an ideal receiving system, which means that all the observation system-related error sources such as the ones mentioned above are neglected in this case. For a more detailed description of the study setup see section 3.

The results are presented as absolute error profiles (geopotential height and temperature) or relative error profiles (bending angle, refractivity, pressure) up to an altitude of 60 km. In this context, error means the (relative) deviation of an observable from the “true” atmospheric conditions as they are provided by the MSIS model. This model was used for forward modeling of the GNSS signals (see section 3.2). The “true” total bending angles were directly computed by the applied 3D ray-tracing algorithm.

Each page contains 12 panels (3 columns, 4 rows), which show the retrieval error results for one of the three representative occultation events (see sections 3.4) for one observable. Given 3 cases and 5 observables displayed, this adds up to 15 pages in each Appendix.

The three columns illustrate different methods of statistical optimization applied in the retrieval. In column 1, the results from the retrieval without statistical optimization (exponential extrapolation) are illustrated. In columns 2 and 3, the results from the retrieval with heuristic optimization (without a priori profile search) and inverse covariance matrix weighting (with a priori profile search) are shown, respectively. For a description of these statistical optimization methods, see section 2.

The four rows represent the retrieval results for different ionospheric conditions: Row 1 shows the retrieval results from a strictly neutral model atmosphere (no ionosphere), while rows 2 to 4 illustrate results from different ionization-levels, driven by the index for the radio flux at 10.7 cm ($F_{10.7}$ index). The $F_{10.7}$ index ranges from $F_{10.7} = 70$ (row 2) via $F_{10.7} = 140$ (row 3) to $F_{10.7} = 210$ (row 4), representing low, middle, and high solar activity ionization levels, respectively.

On top of each individual plot panel two measures of quality referring to the average error estimate in the 35 to 45 km height interval are given: The bias, which describes the mean deviation of the retrieved profile from the “true” profile in this interval, and the standard deviation (stddev), which describes the mean fluctuation of the bias-corrected retrieved profile in the same interval.

A.1. Bending Angle

NICE EVENT

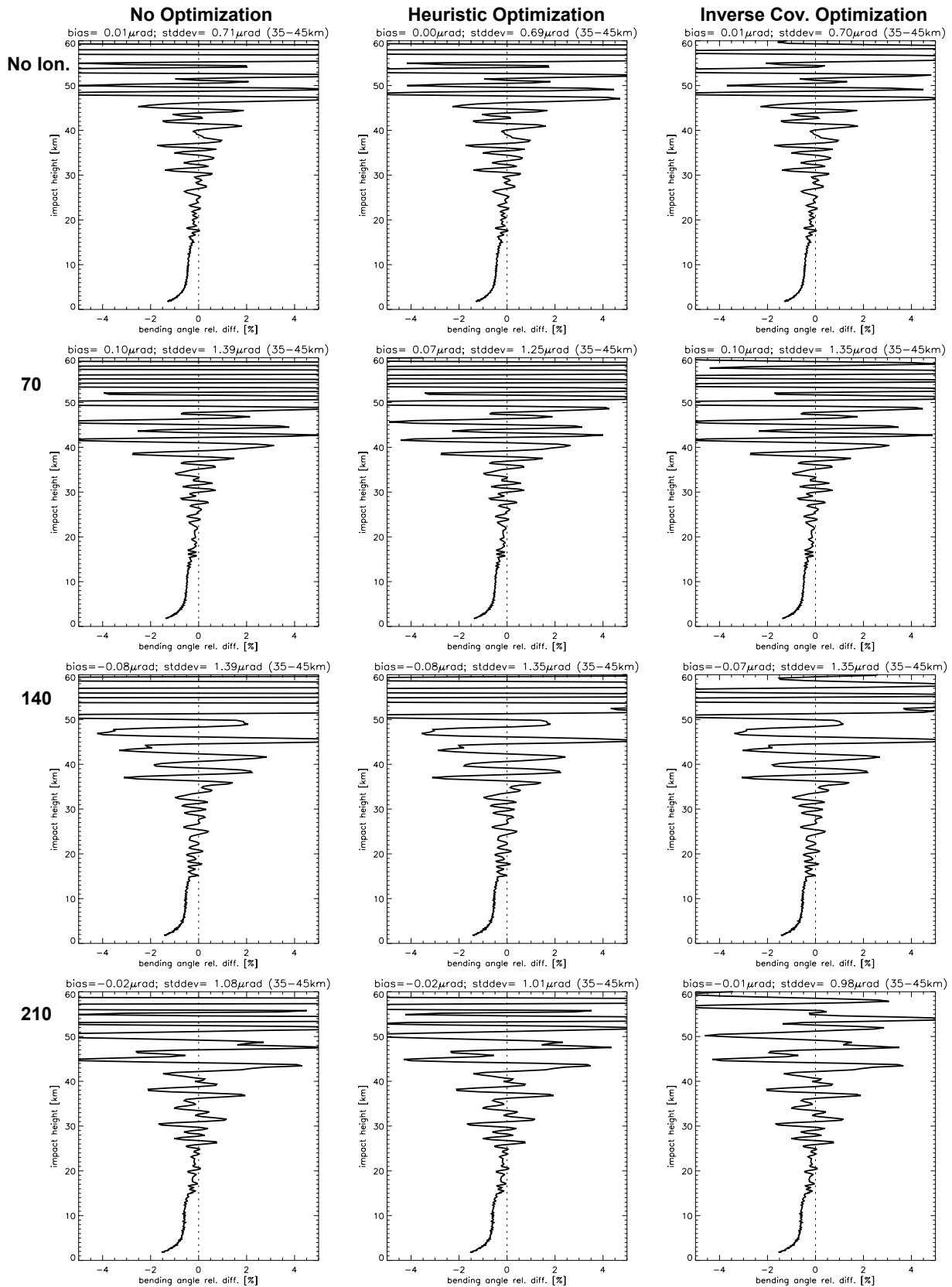


Figure A.1.1: Relative difference between retrieved and “true” bending angle. Event case: Nice event.

NASTY 1 EVENT

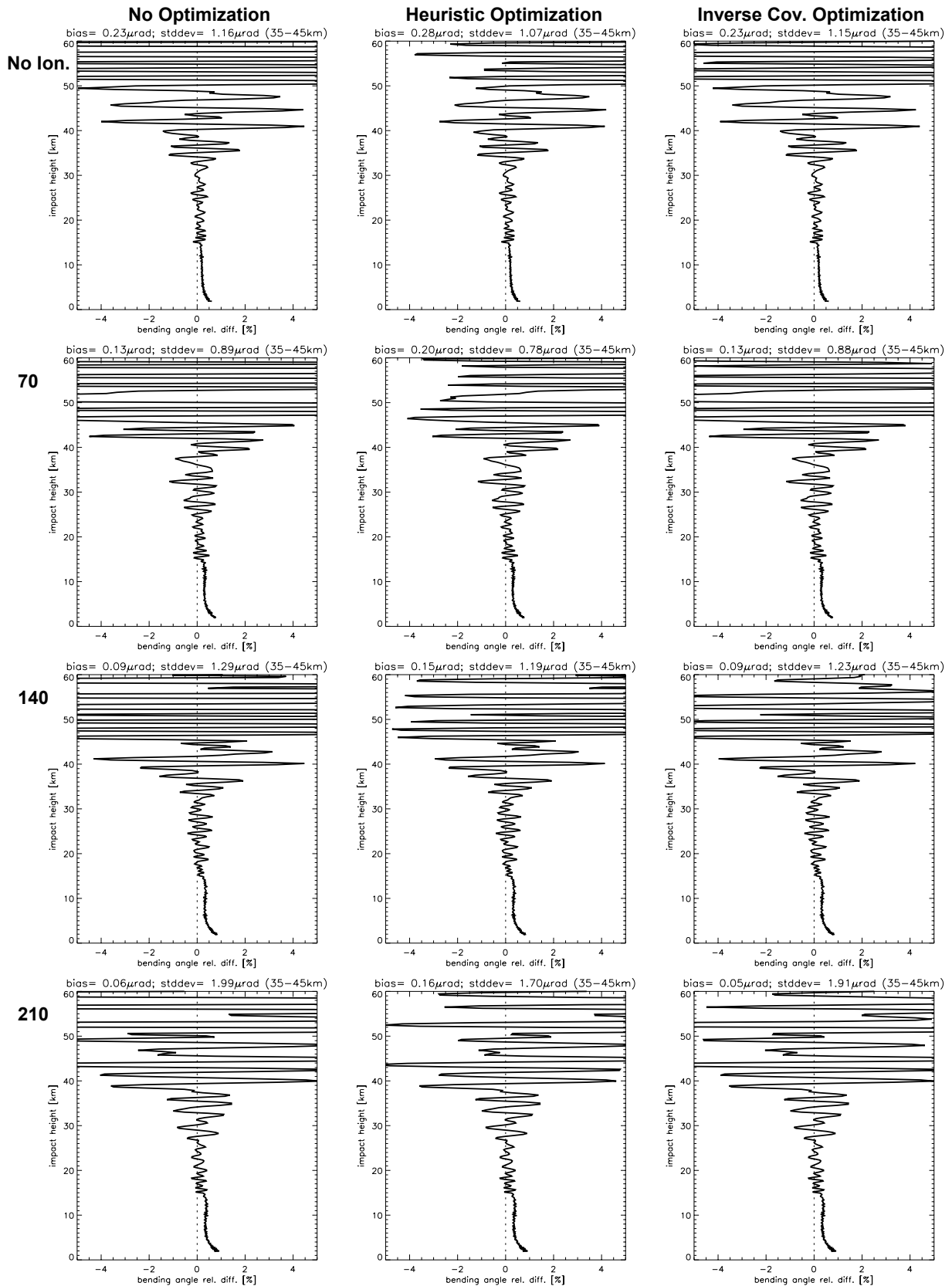


Figure A.1.2: Relative difference between retrieved and "true" bending angle. Event case: Nasty 1 event.

NASTY 2 EVENT

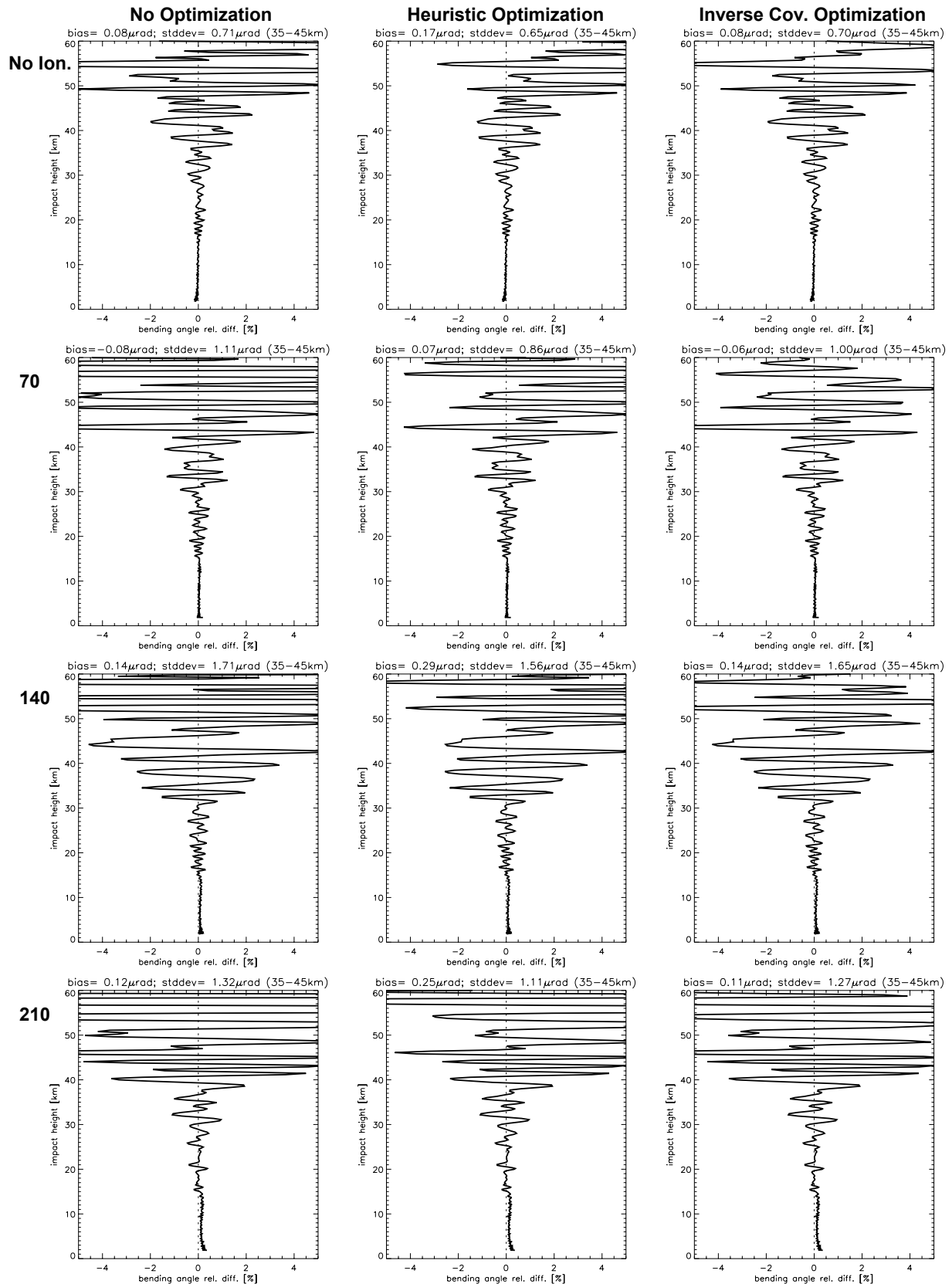


Figure A.1.3: Relative difference between retrieved and “true” bending angle. Event case: Nasty 2 event.

A.2. Refractivity

NICE EVENT

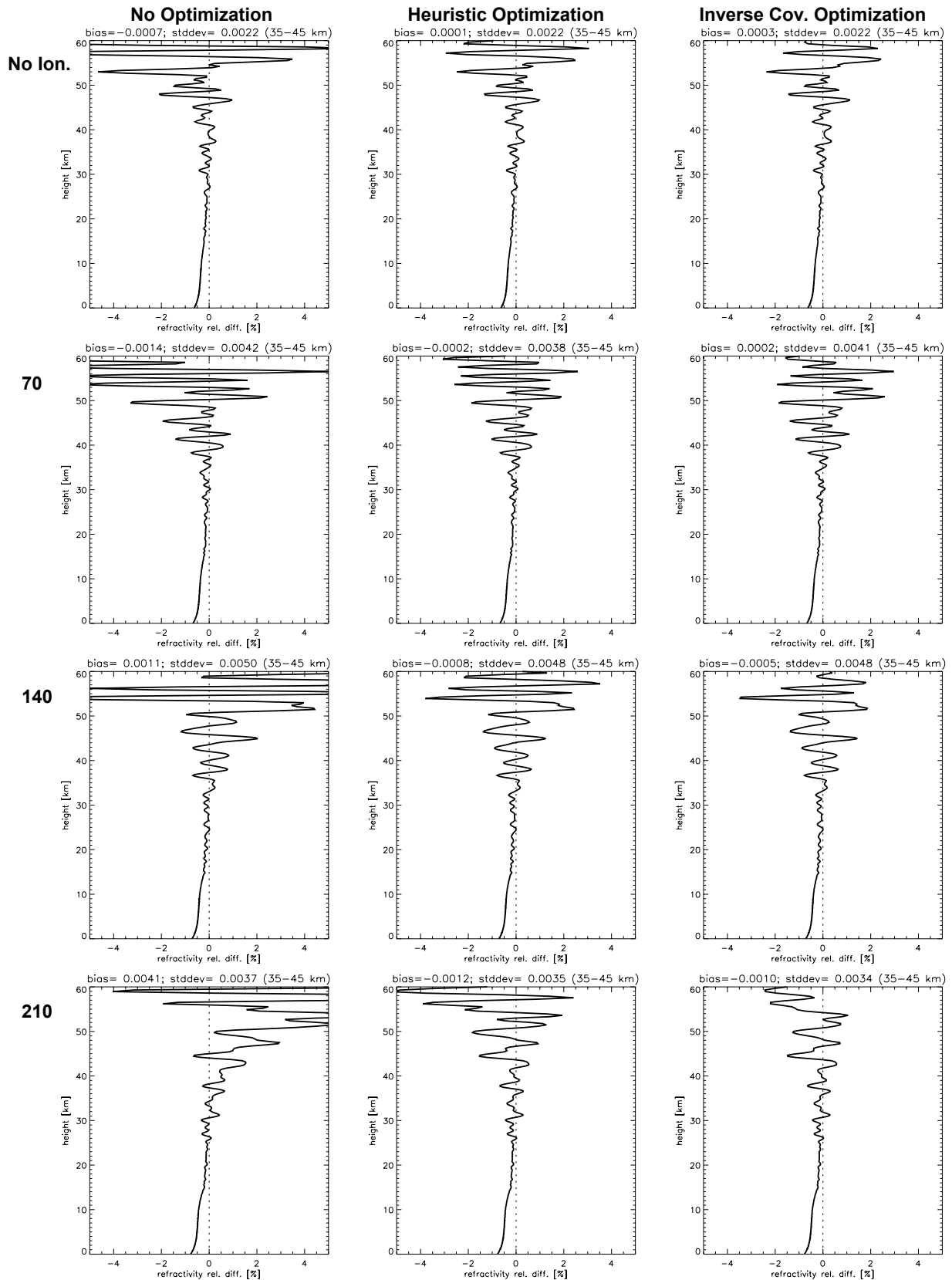


Figure A.2.1: Relative difference between retrieved and "true" refractivity. Bias and standard deviation between 35 and 45 km are given in N units. Event case: Nice Event.

NASTY 1 EVENT

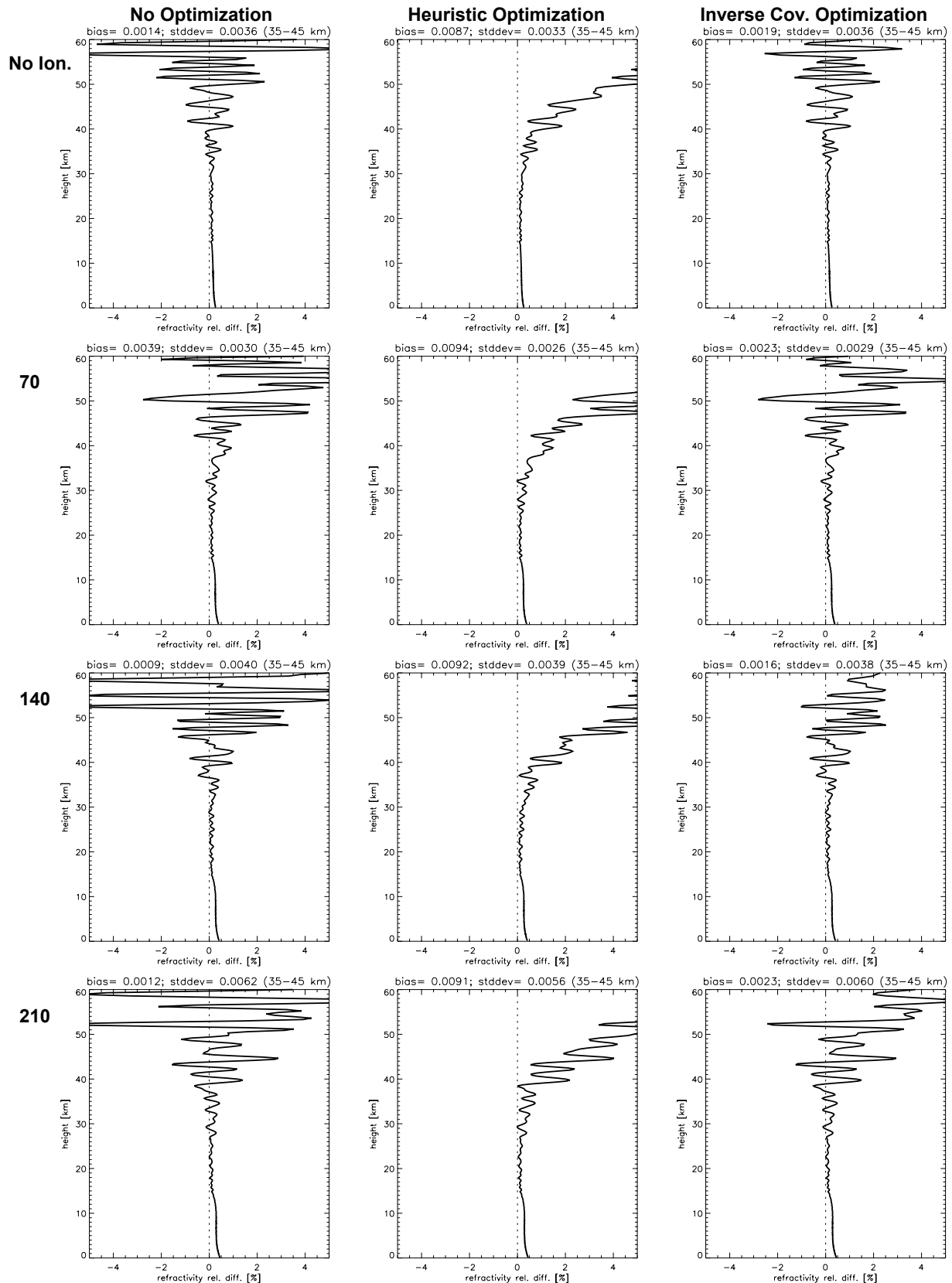


Figure A.2.2: Relative difference between retrieved and "true" refractivity. Bias and standard deviation between 35 and 45 km are given in N units. Event case: Nasty 1 event.

NASTY 2 EVENT

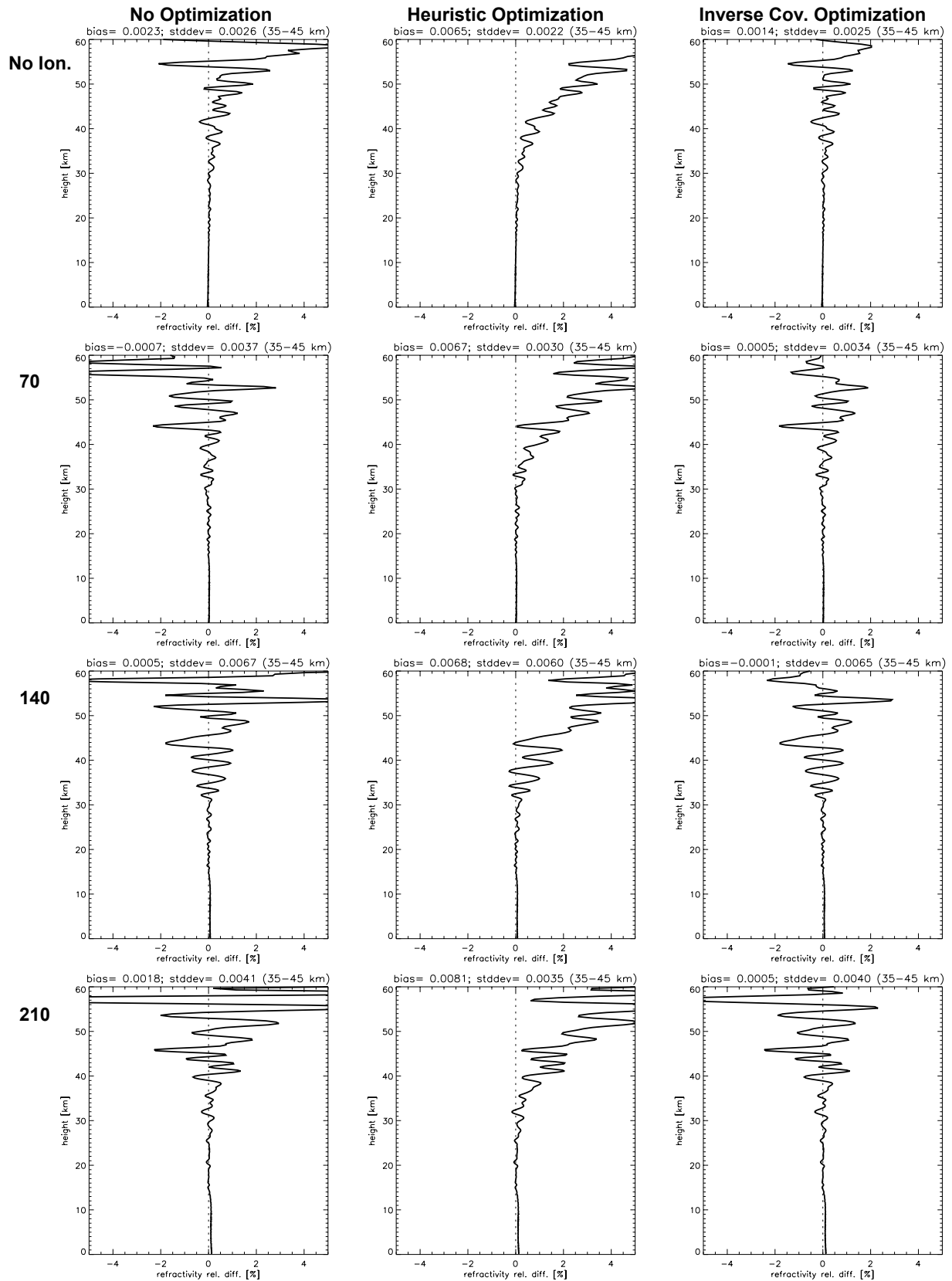


Figure A.2.3: Relative difference between retrieved and “true” refractivity. Bias and standard deviation between 35 and 45 km are given in N units. Event case: Nasty 2 event.

A.3. Pressure

NICE EVENT

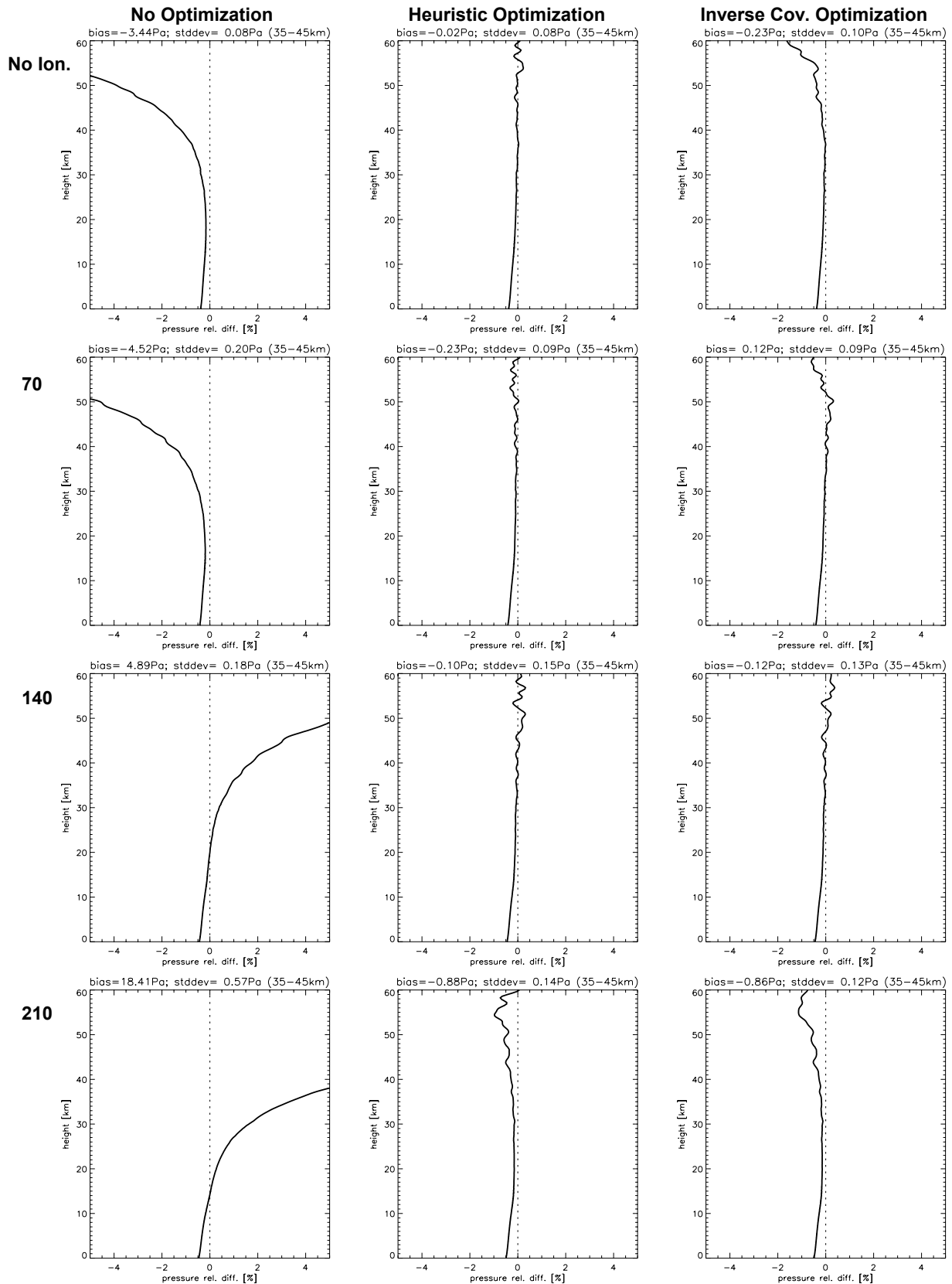


Figure A.3.1: Relative difference between retrieved and "true" pressure. Event case: Nice event.

NASTY 1 EVENT

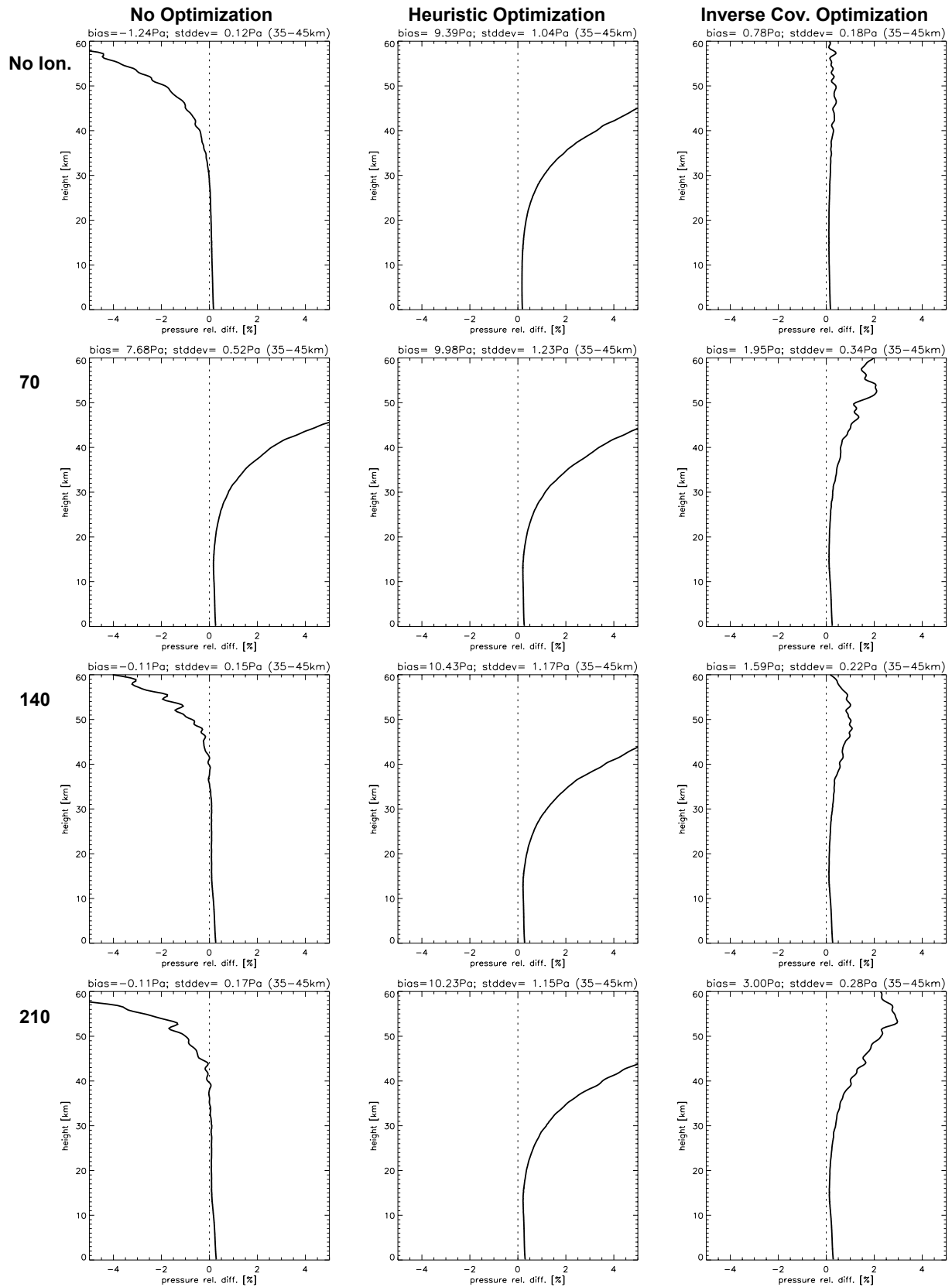


Figure A.3.2: Relative difference between retrieved and “true” pressure. Event case: Nasty 1 event.

NASTY 2 EVENT

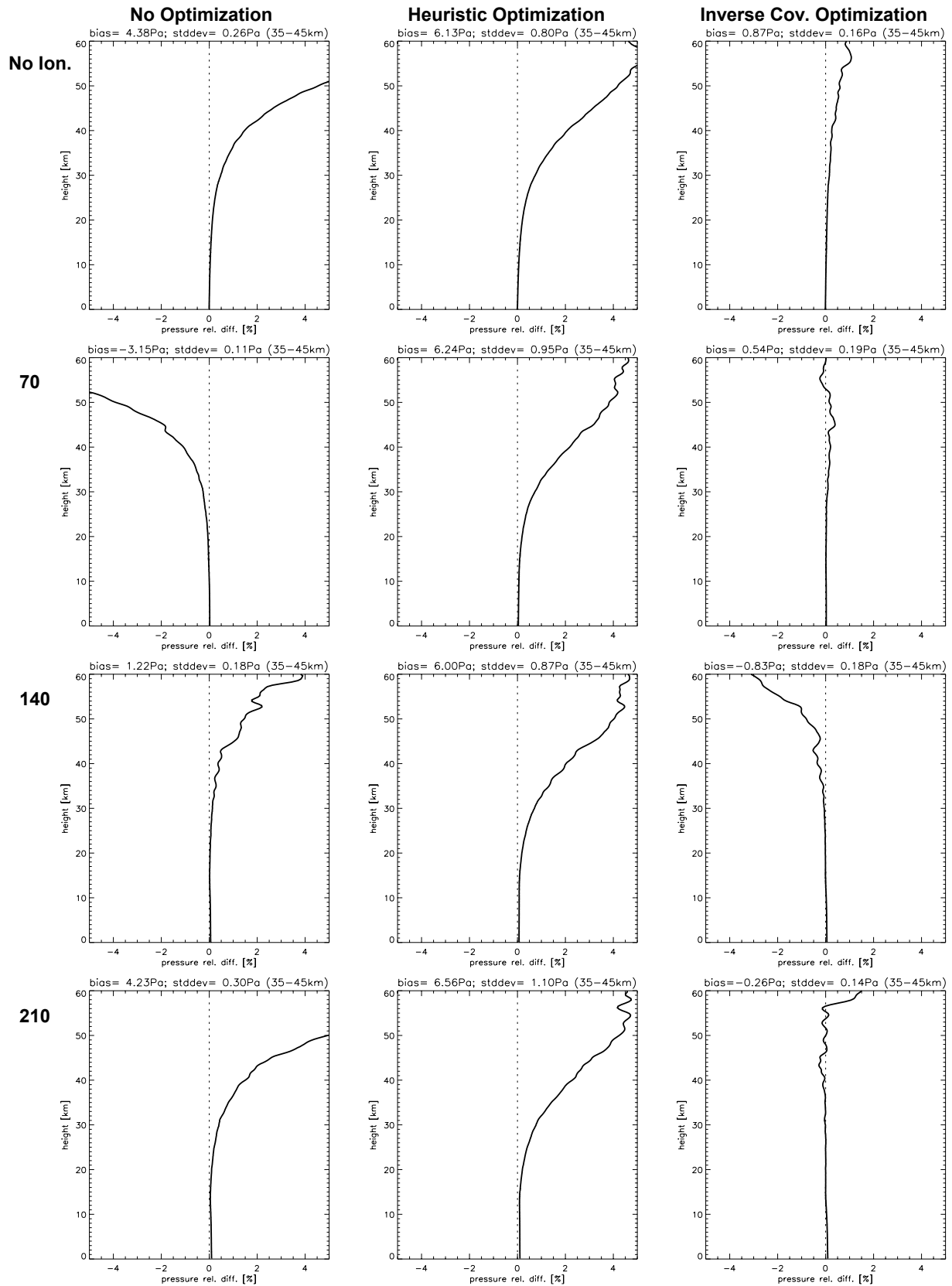


Figure A.3.3: Relative difference between retrieved and "true" pressure. Event case: Nasty 2 event.

A.4. Geopotential Height

NICE EVENT

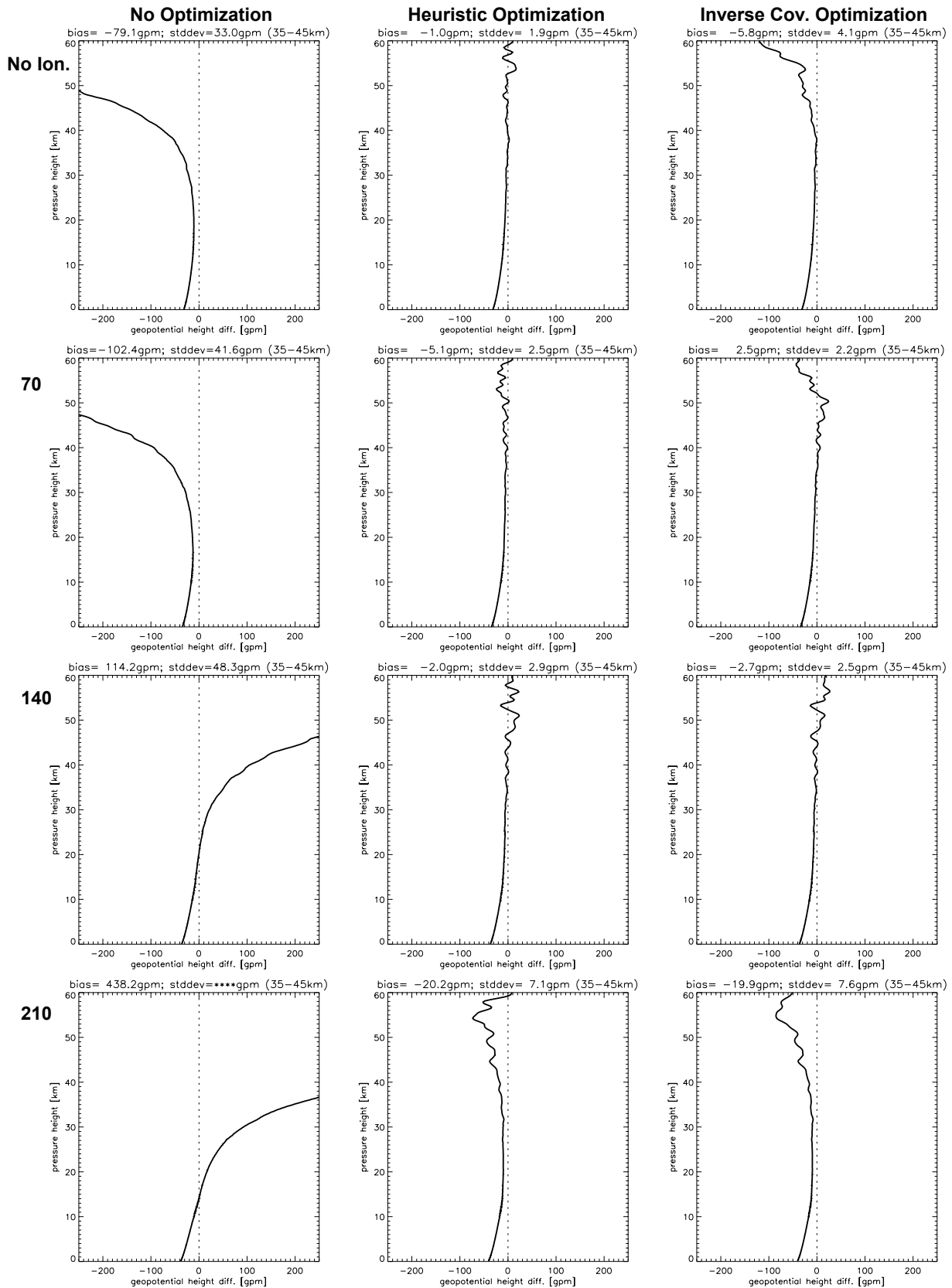


Figure A.4.1: Difference between retrieved and “true” geopotential height. Event case: Nice event.

NASTY 1 EVENT

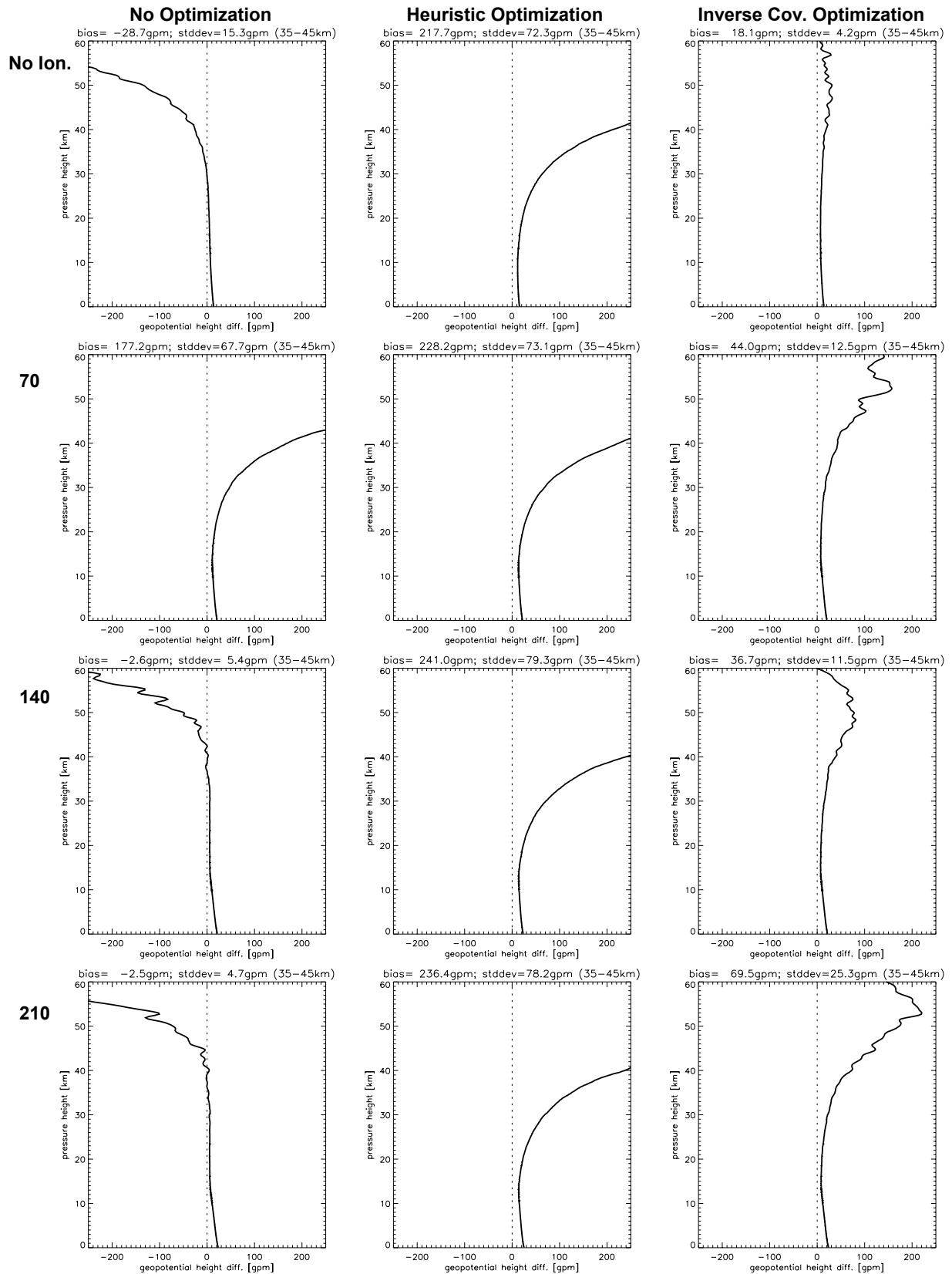


Figure A.4.2: Difference between retrieved and “true” geopotential height. Event case: Nasty 1 event.

NASTY 2 EVENT

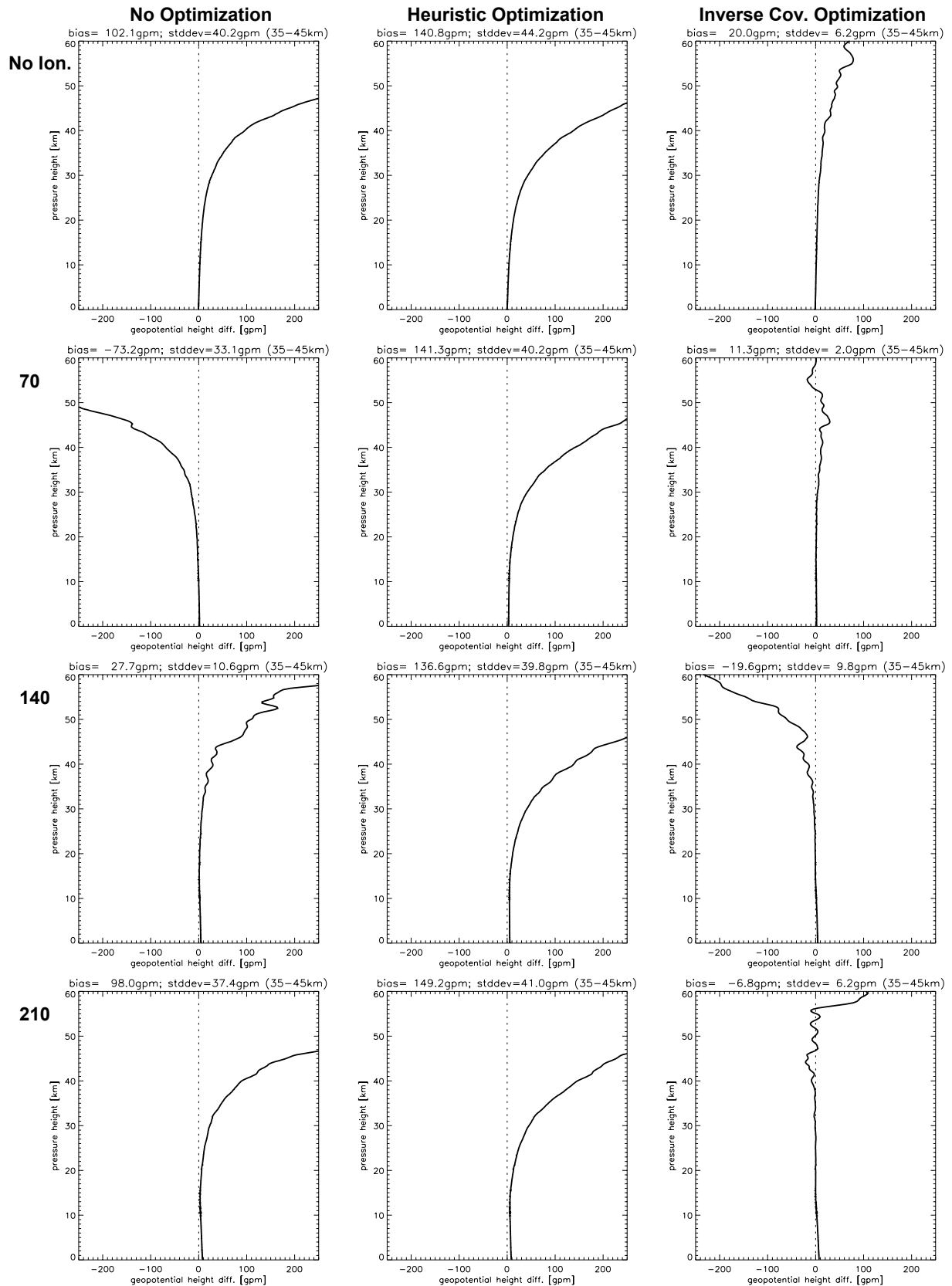


Figure A.4.3: Difference between retrieved and "true" geopotential height. Event case: Nasty 2 event.

A.5. Temperature

NICE EVENT

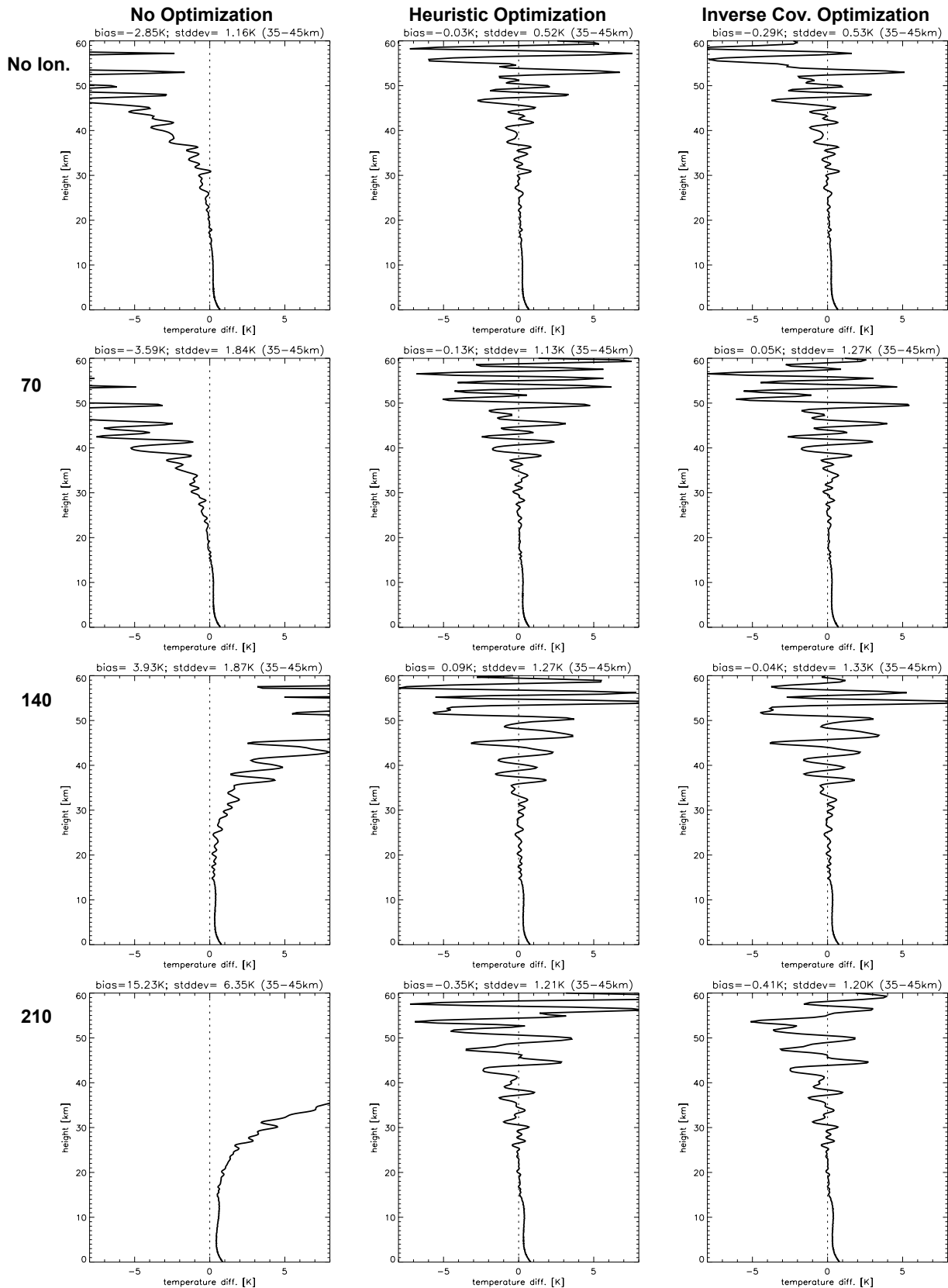


Figure A.5.1: Difference between retrieved and “true” temperature. Event case: Nice event.

NASTY 1 EVENT

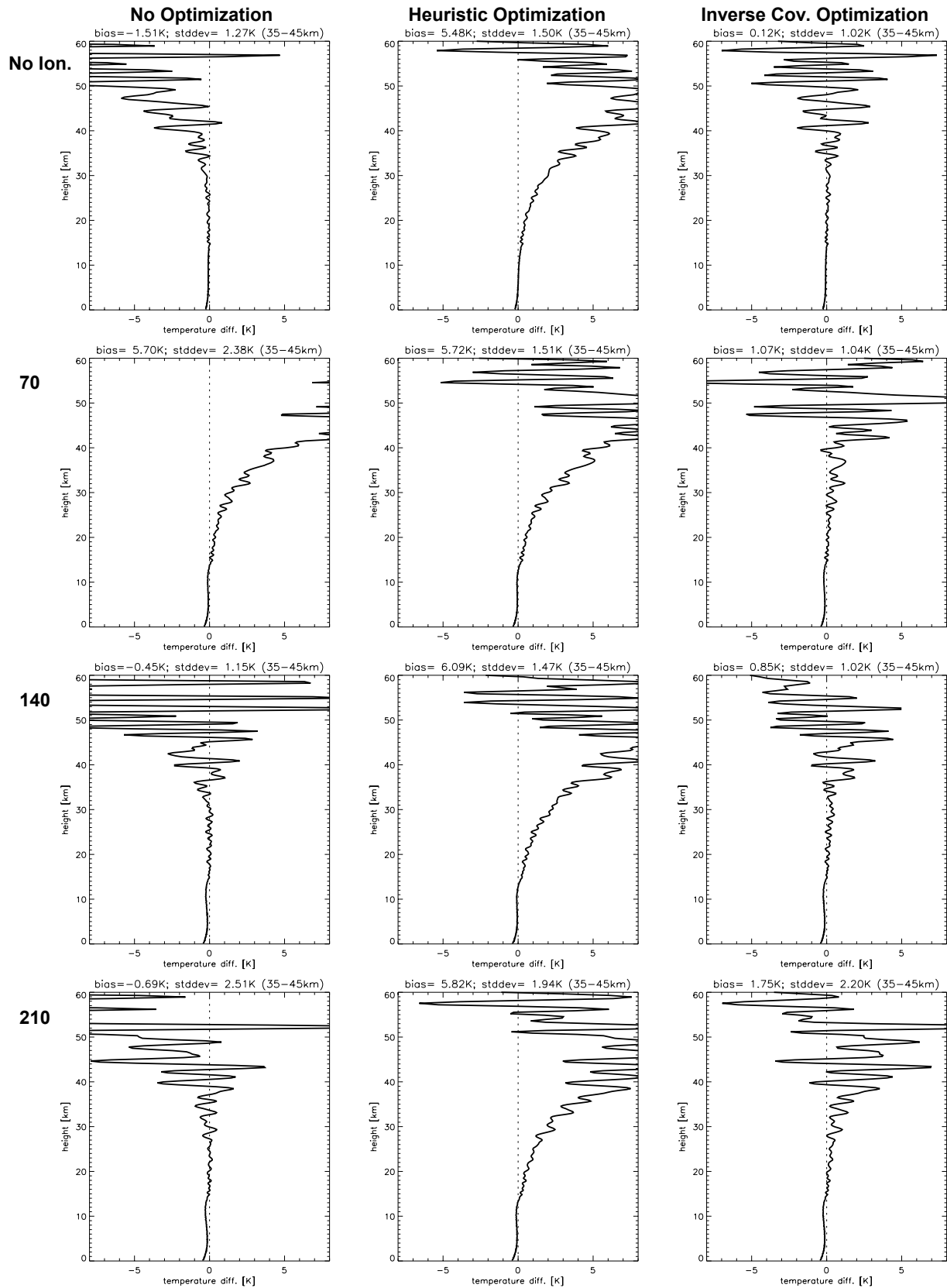


Figure A.5.2: Difference between retrieved and "true" temperature. Event case: Nasty 1 event.

NASTY 2 EVENT

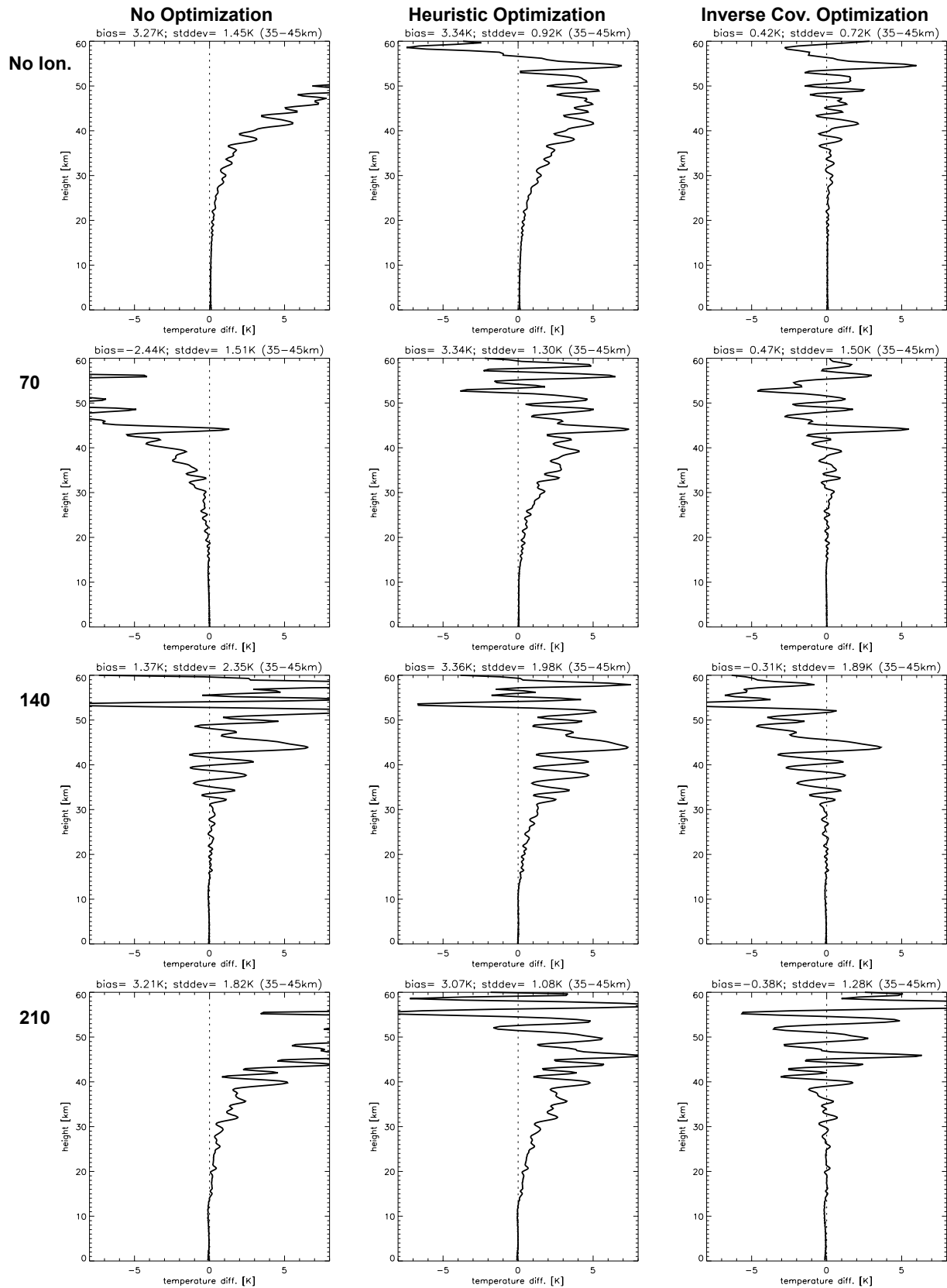


Figure A.5.3: Difference between retrieved and "true" temperature. Event case: Nasty 2 event.

Appendix B. Retrieval Results – Ideal Receiving System

In Appendices A and B we present a comprehensive compilation of the ACCESS WP3200 study results. Appendix A shows the results for a quasi-realistic (METOP/GRAS-like) receiving system including all observation system-related error sources such as orbit uncertainties, receiver noise, local multipath errors and clock errors. Appendix B shows the results for an ideal receiving system, which means that all the observation system-related error sources such as the ones mentioned above are neglected in this case. For a more detailed description of the study setup see section 3.

The results are presented as absolute error profiles (geopotential height and temperature) or relative error profiles (bending angle, refractivity, pressure) up to an altitude of 60 km. In this context, error means the (relative) deviation of an observable from the “true” atmospheric conditions as they are provided by the MSIS model. This model was used for forward modeling of the GNSS signals (see section 3.2). The “true” total bending angles were directly computed by the applied 3D ray-tracing algorithm.

Each page contains 12 panels (3 columns, 4 rows), which show the retrieval error results for one of the three representative occultation events (see sections 3.4) for one observable. Given 3 cases and 5 observables displayed, this adds up to 15 pages in each Appendix.

The three columns illustrate different methods of statistical optimization applied in the retrieval. In column 1, the results from the retrieval without statistical optimization (exponential extrapolation) are illustrated. In columns 2 and 3, the results from the retrieval with heuristic optimization (without a priori profile search) and inverse covariance matrix weighting (with a priori profile search) are shown, respectively. For a description of these statistical optimization methods, see section 2.

The four rows represent the retrieval results for different ionospheric conditions: Row 1 shows the retrieval results from a strictly neutral model atmosphere (no ionosphere), while rows 2 to 4 illustrate results from different ionization-levels, driven by the index for the radio flux at 10.7 cm ($F_{10.7}$ index). The $F_{10.7}$ index ranges from $F_{10.7} = 70$ (row 2) via $F_{10.7} = 140$ (row 3) to $F_{10.7} = 210$ (row 4), representing low, middle, and high solar activity ionization levels, respectively.

On top of each individual plot panel two measures of quality referring to the average error estimate in the 35 to 45 km height interval are given: The bias, which describes the mean deviation of the retrieved profile from the “true” profile in this interval, and the standard deviation (stddev), which describes the mean fluctuation of the bias-corrected retrieved profile in the same interval.

B.1. Bending Angle

NICE EVENT

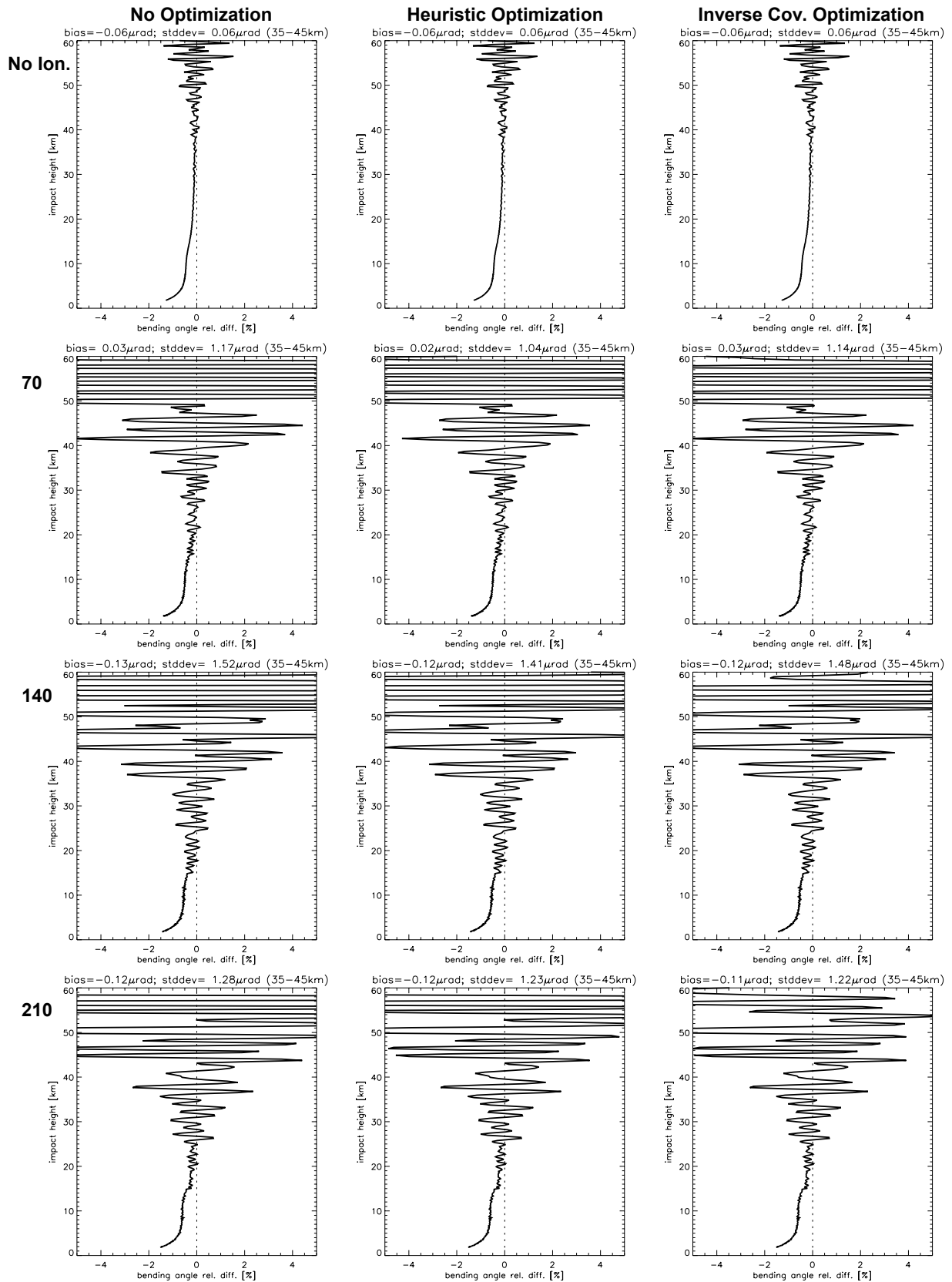


Figure B.1.1: Relative difference between retrieved and “true” bending angle. Event case: Nice event.

NASTY 1 EVENT

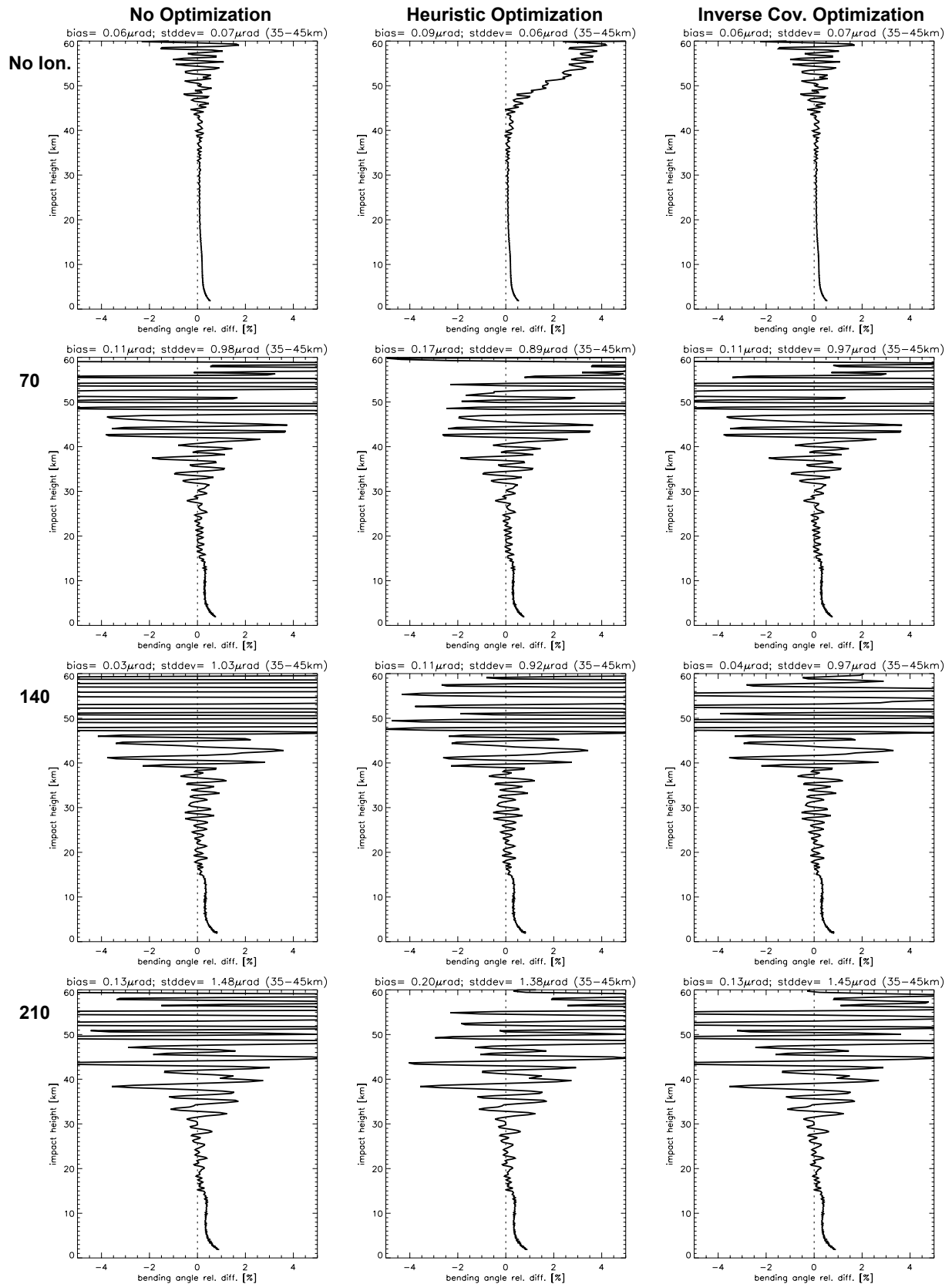


Figure B.1.2: Relative difference between retrieved and "true" bending angle. Event case: Nasty 1 event.

NASTY 2 EVENT

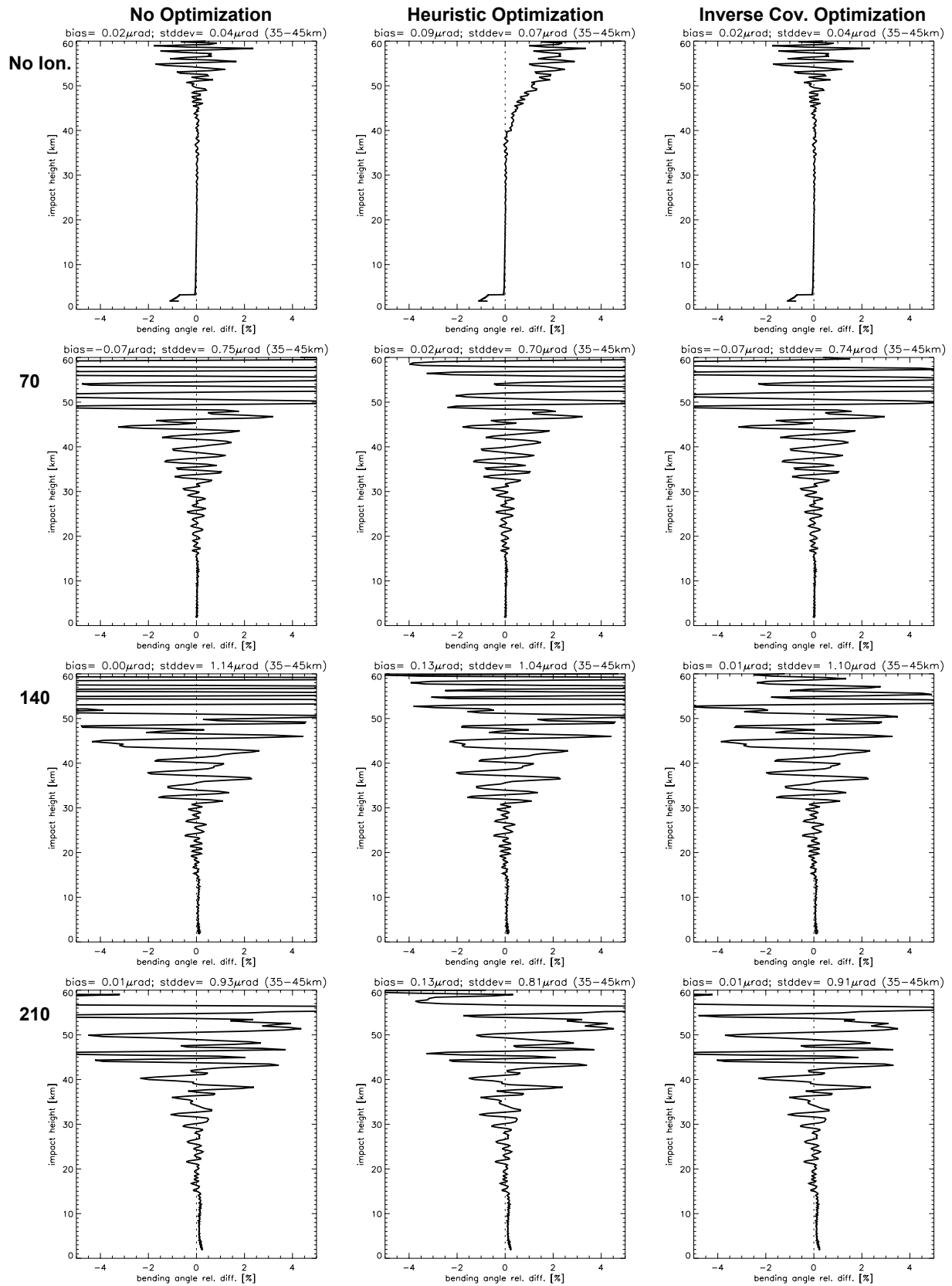


Figure B.1.3: Relative difference between retrieved and “true” bending angle. Event case: Nasty 2 event.

B.2. Refractivity

NICE EVENT

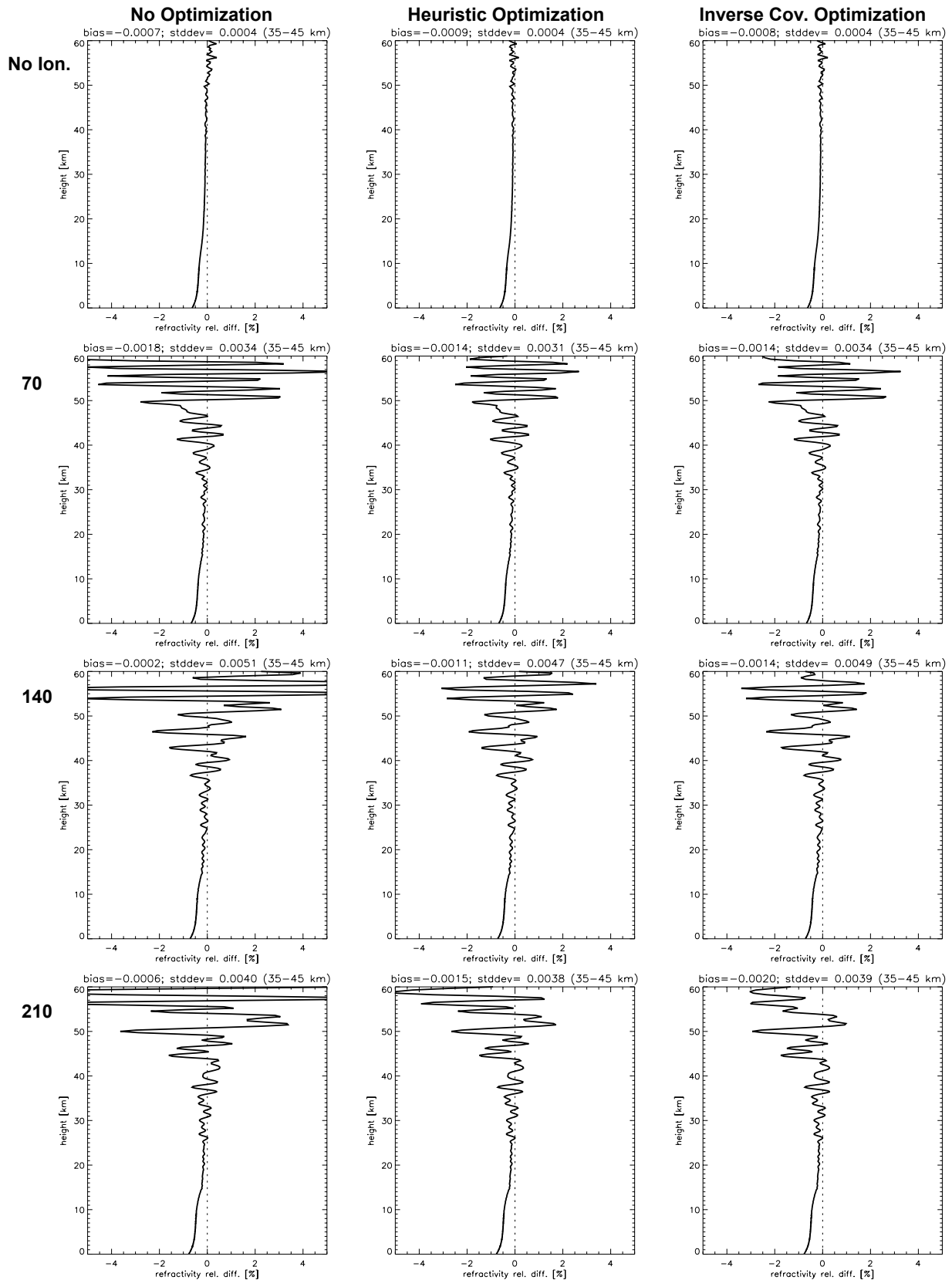


Figure B.2.1: Relative difference between retrieved and “true” refractivity. Bias and standard deviation between 35 and 45 km are given in N units. Event case: Nice Event.

NASTY 1 EVENT

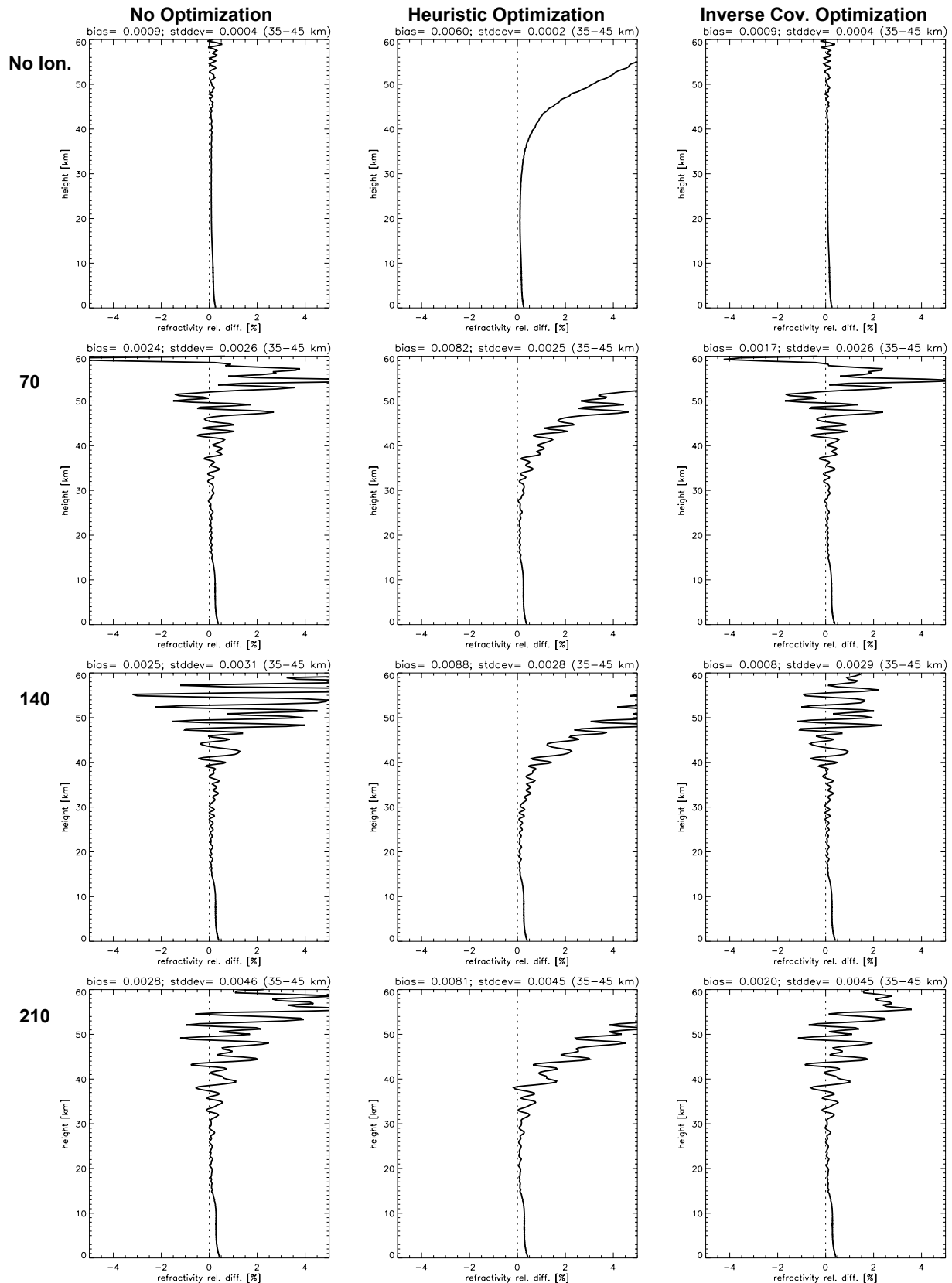


Figure B.2.2: Relative difference between retrieved and "true" refractivity. Bias and standard deviation between 35 and 45 km are given in N units. Event case: Nasty 1 event.

NASTY 2 EVENT

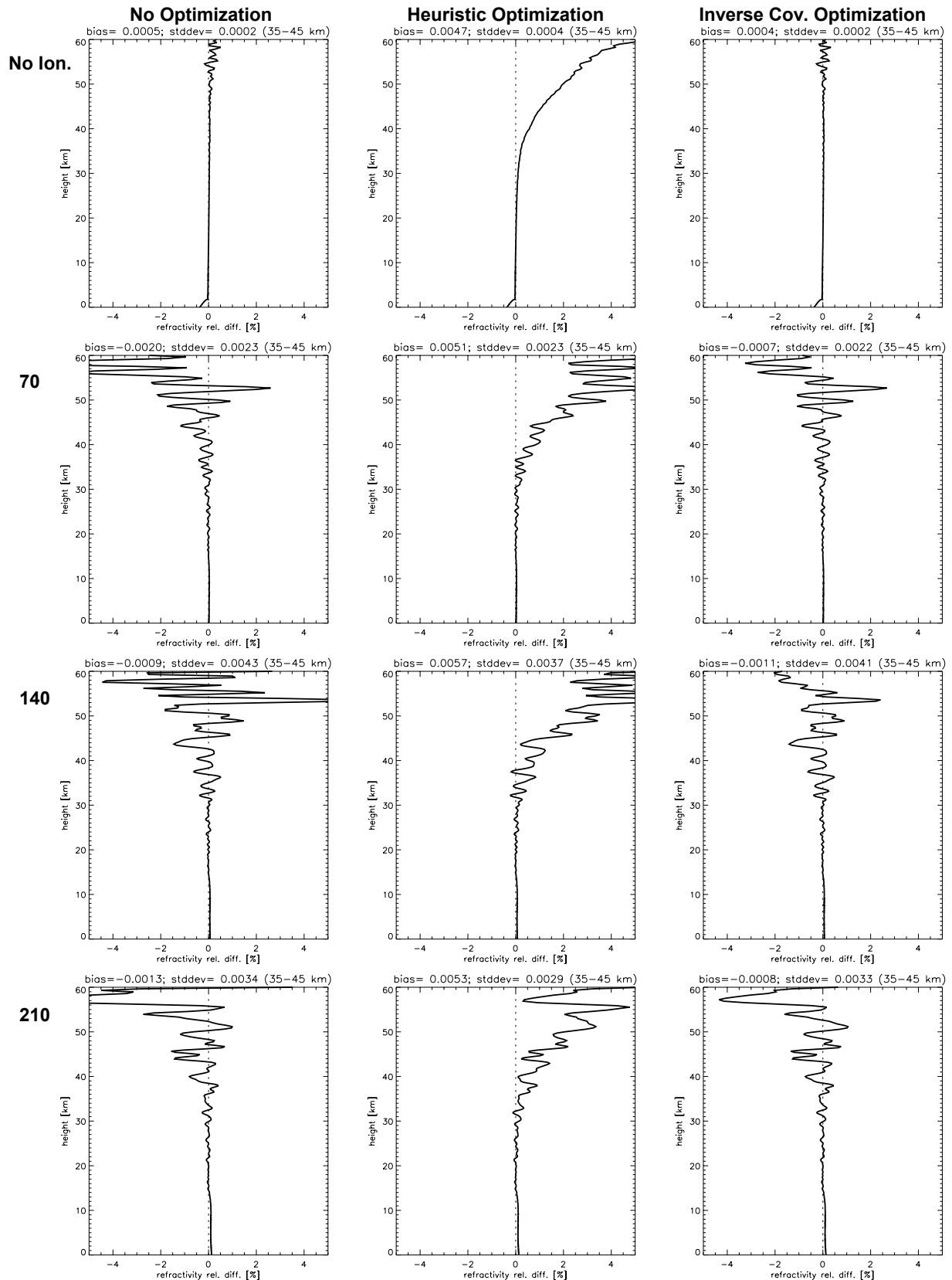


Figure B.2.3: Relative difference between retrieved and "true" refractivity. Bias and standard deviation between 35 and 45 km are given in N units. Event case: Nasty 2 event.

B.3. Pressure

NICE EVENT

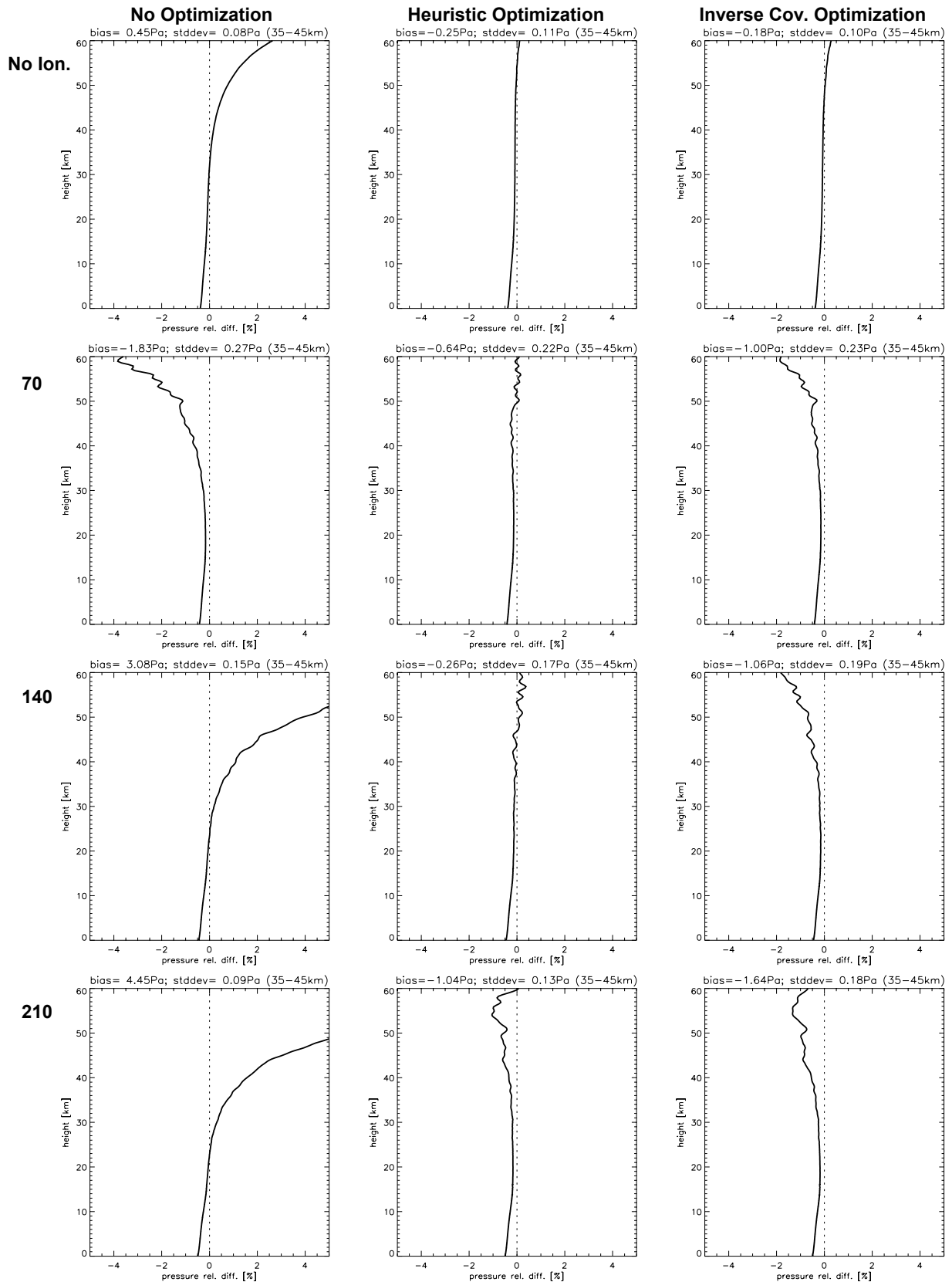


Figure B.3.1: Relative difference between retrieved and "true" pressure. Event case: Nice event.

NASTY 1 EVENT

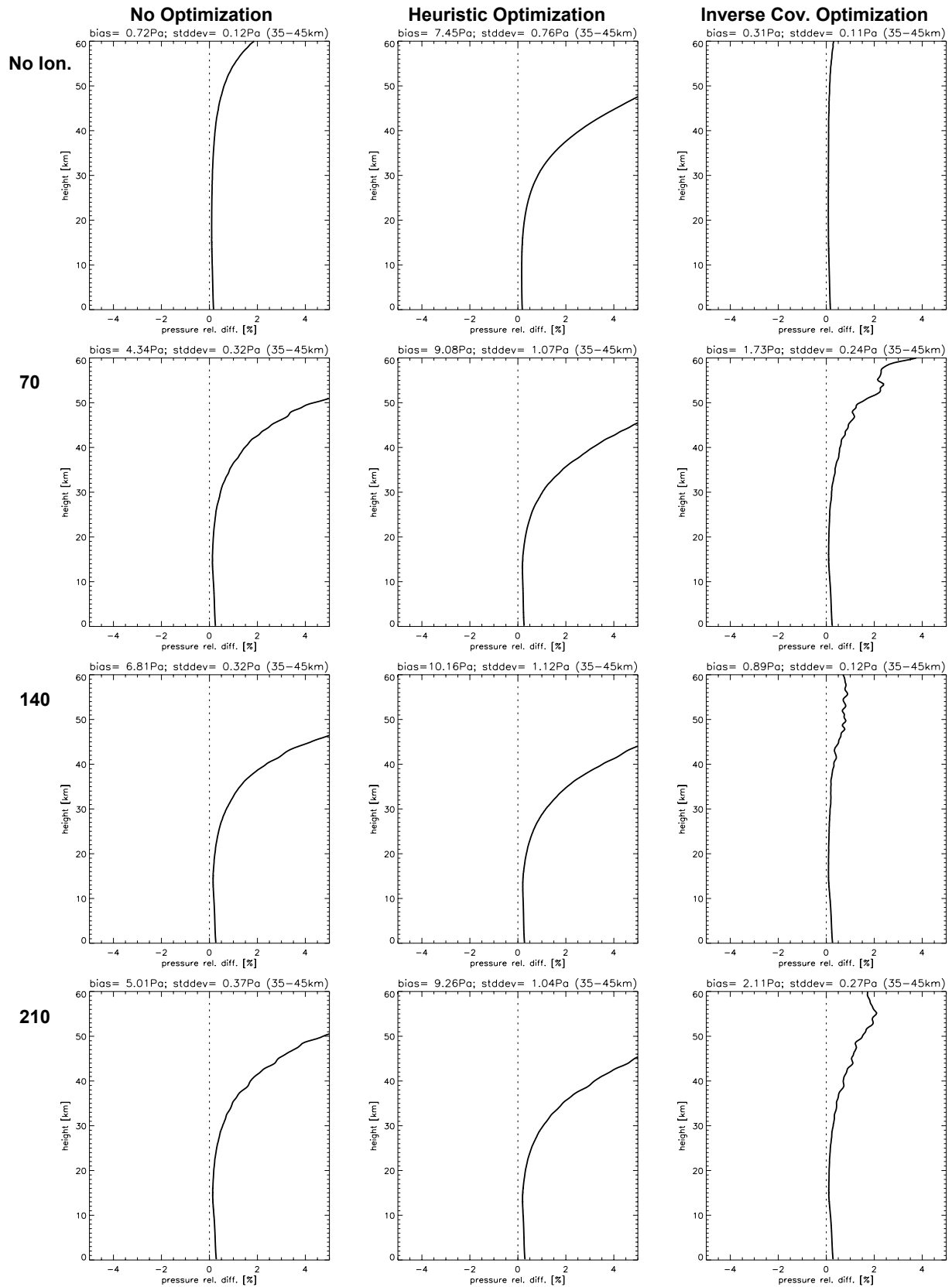


Figure B.3.2: Relative difference between retrieved and “true” pressure. Event case: Nasty 1 event.

NASTY 2 EVENT

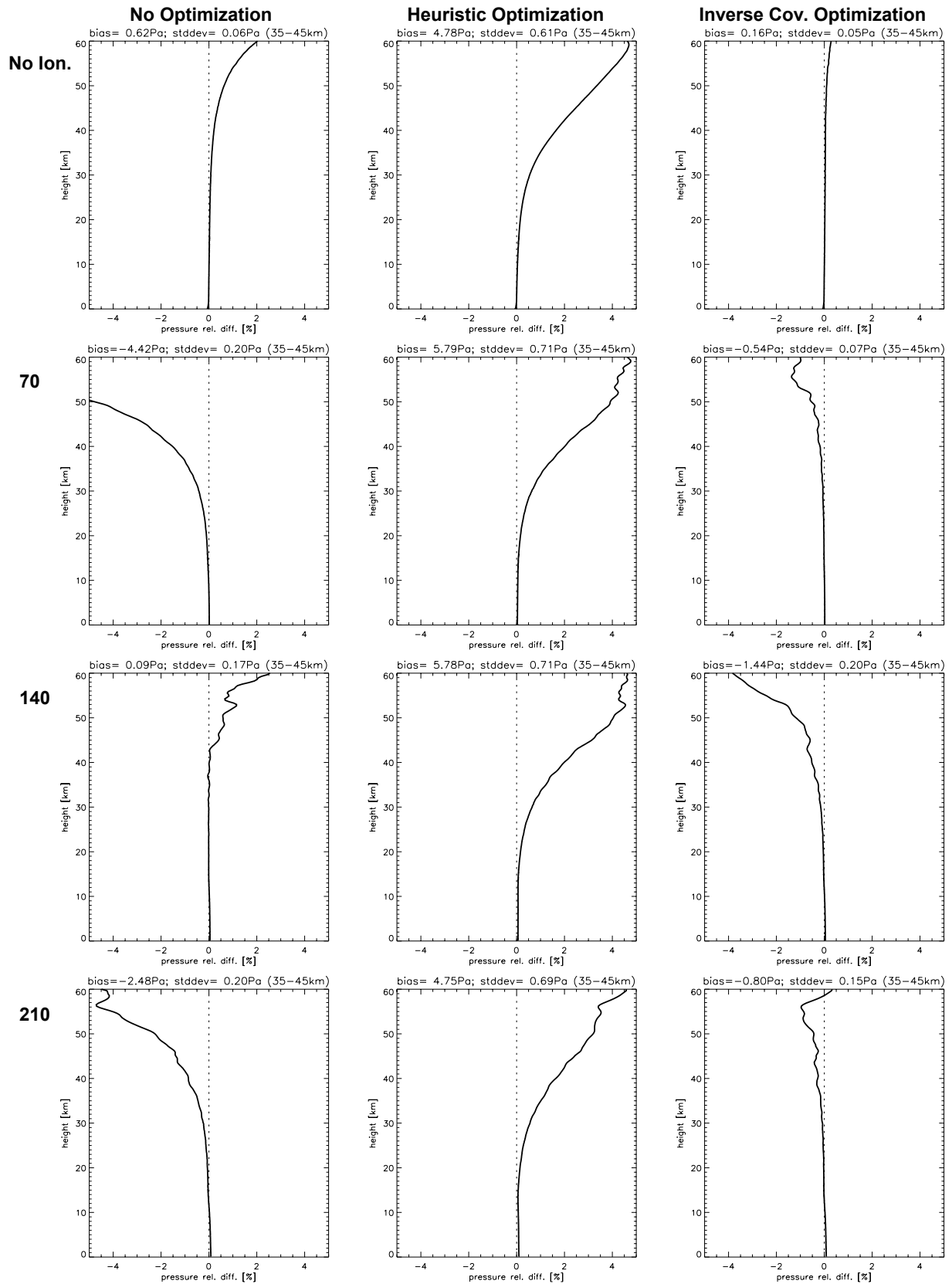


Figure B.3.3: Relative difference between retrieved and "true" pressure. Event case: Nasty 2 event.

B.4. Geopotential Height

NICE EVENT

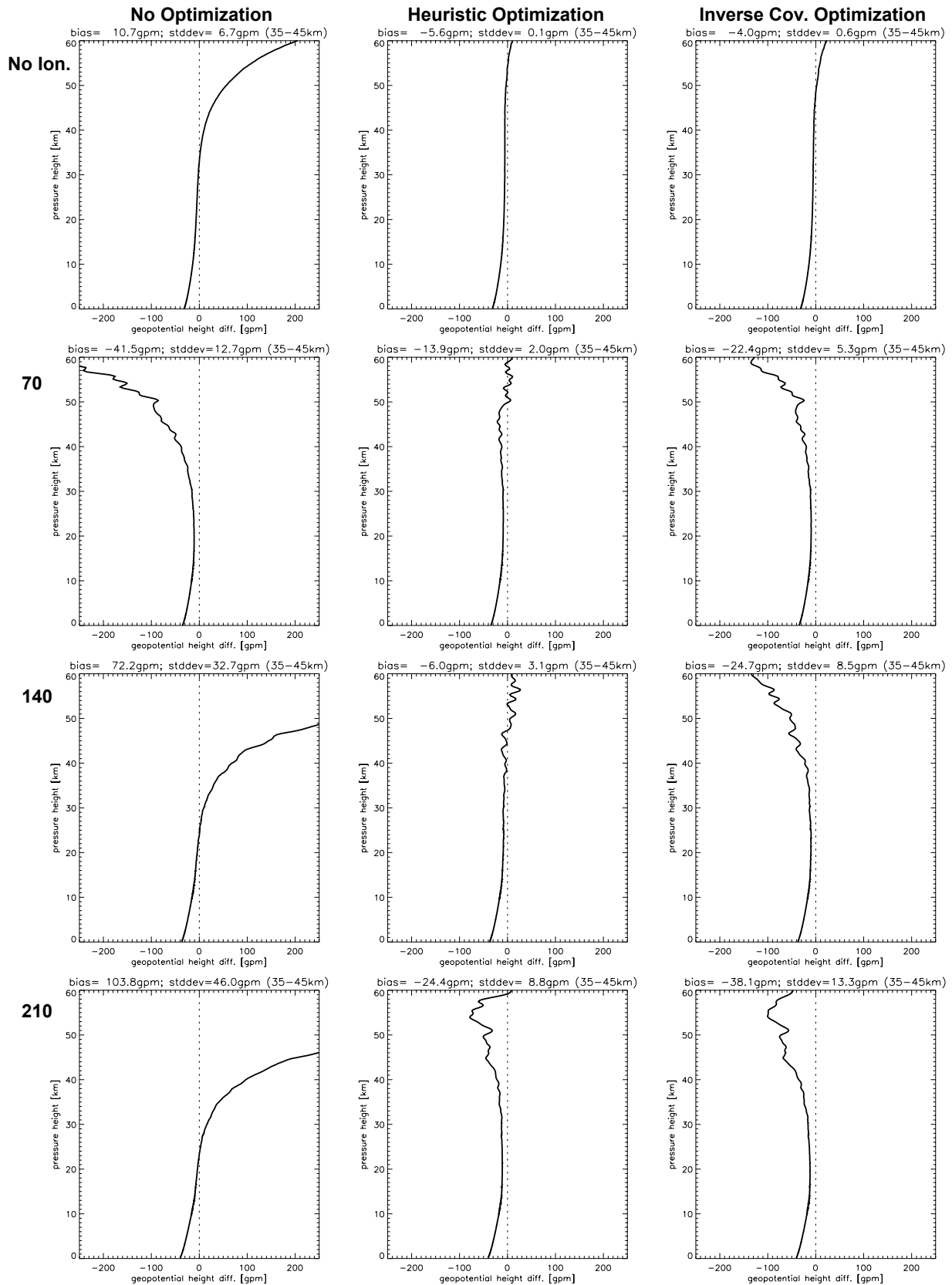


Figure B.4.1: Difference between retrieved and “true” geopotential height. Event case: Nice event.

NASTY 1 EVENT

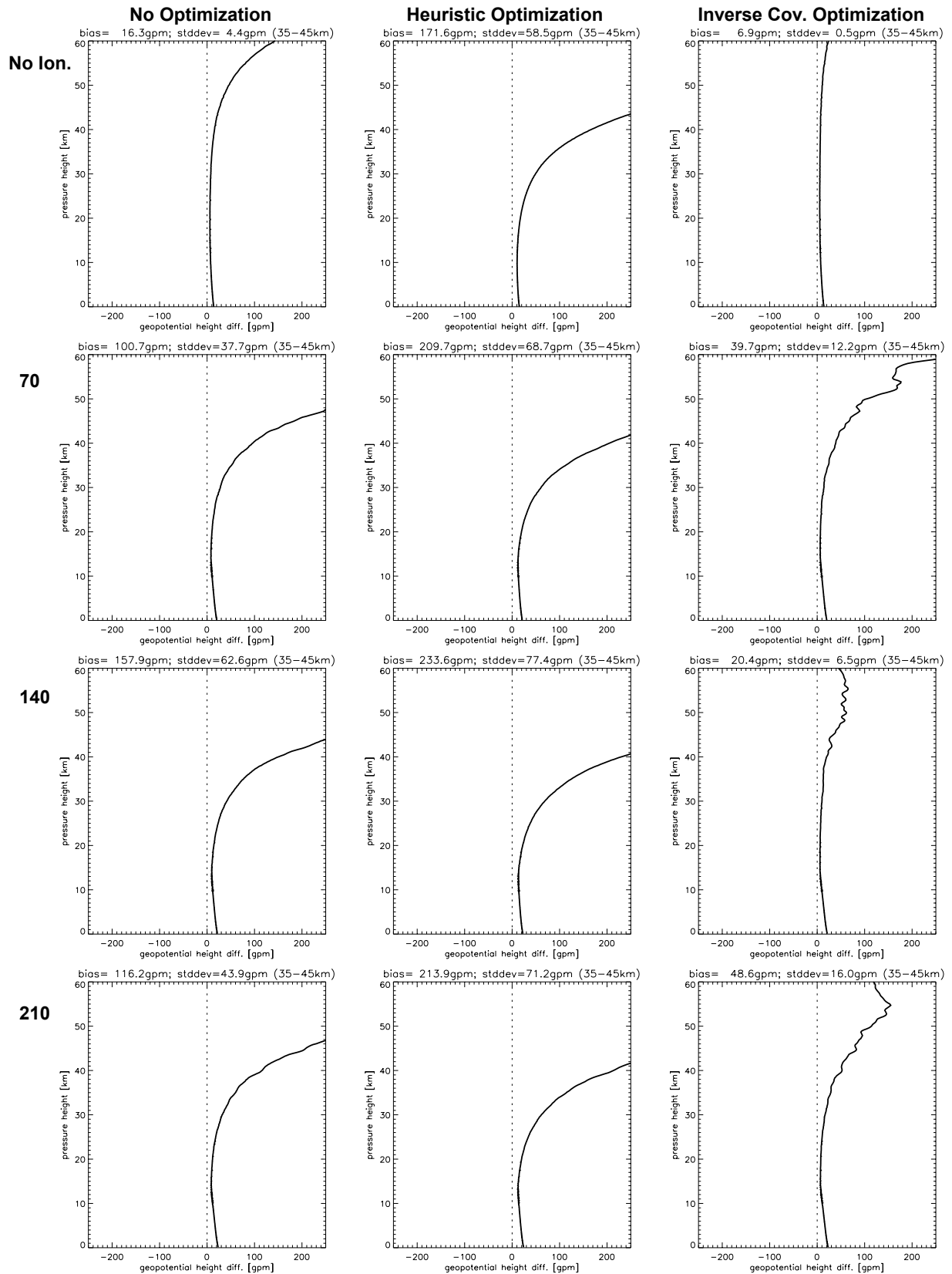


Figure B.4.2: Difference between retrieved and "true" geopotential height. Event case: Nasty 1 event.

NASTY 2 EVENT

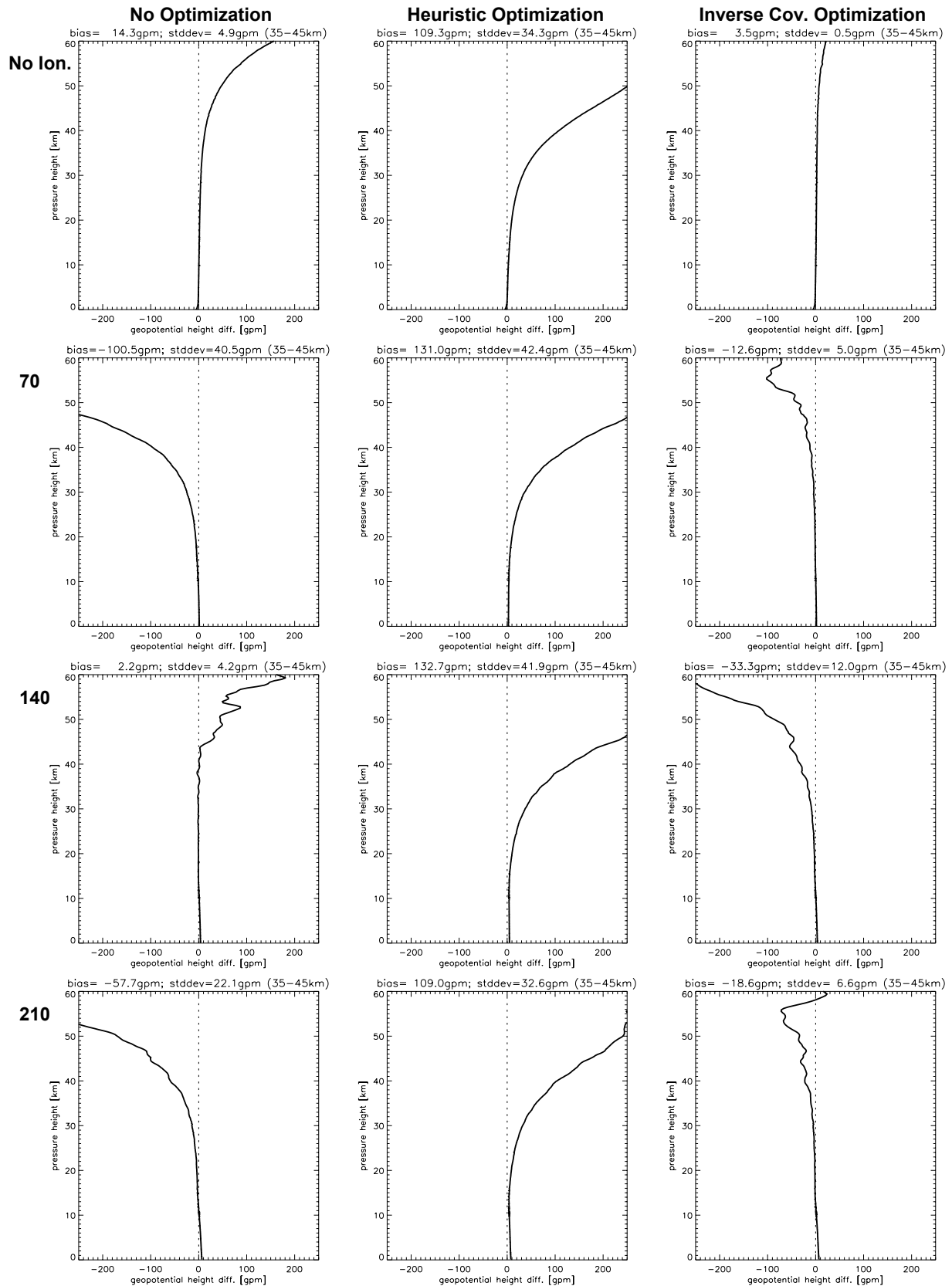


Figure B.4.3: Difference between retrieved and “true” geopotential height. Event case: Nasty 2 event.

B.5. Temperature

NICE EVENT

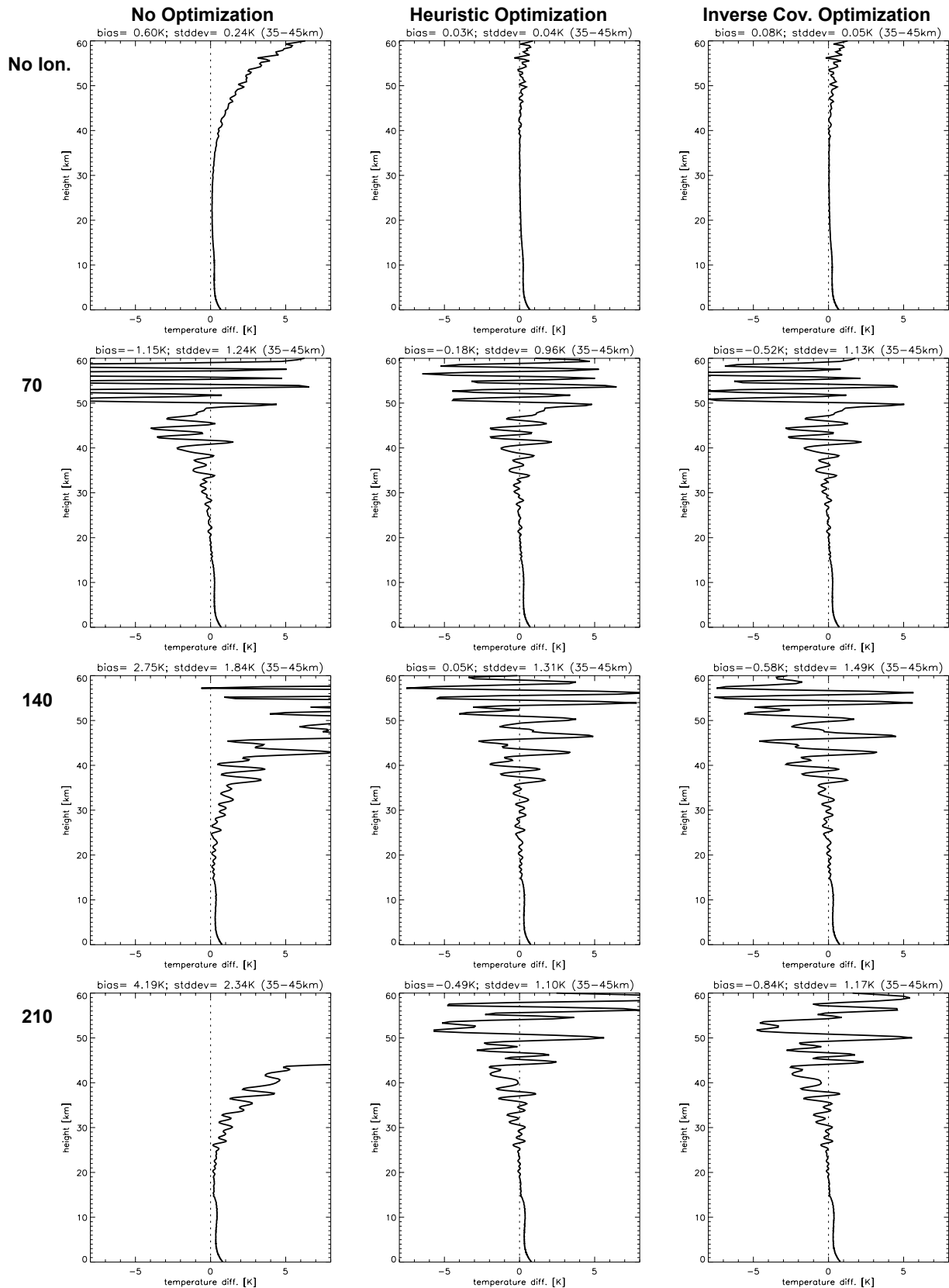


Figure B.5.1: Difference between retrieved and "true" temperature. Event case: Nice event.

NASTY 1 EVENT

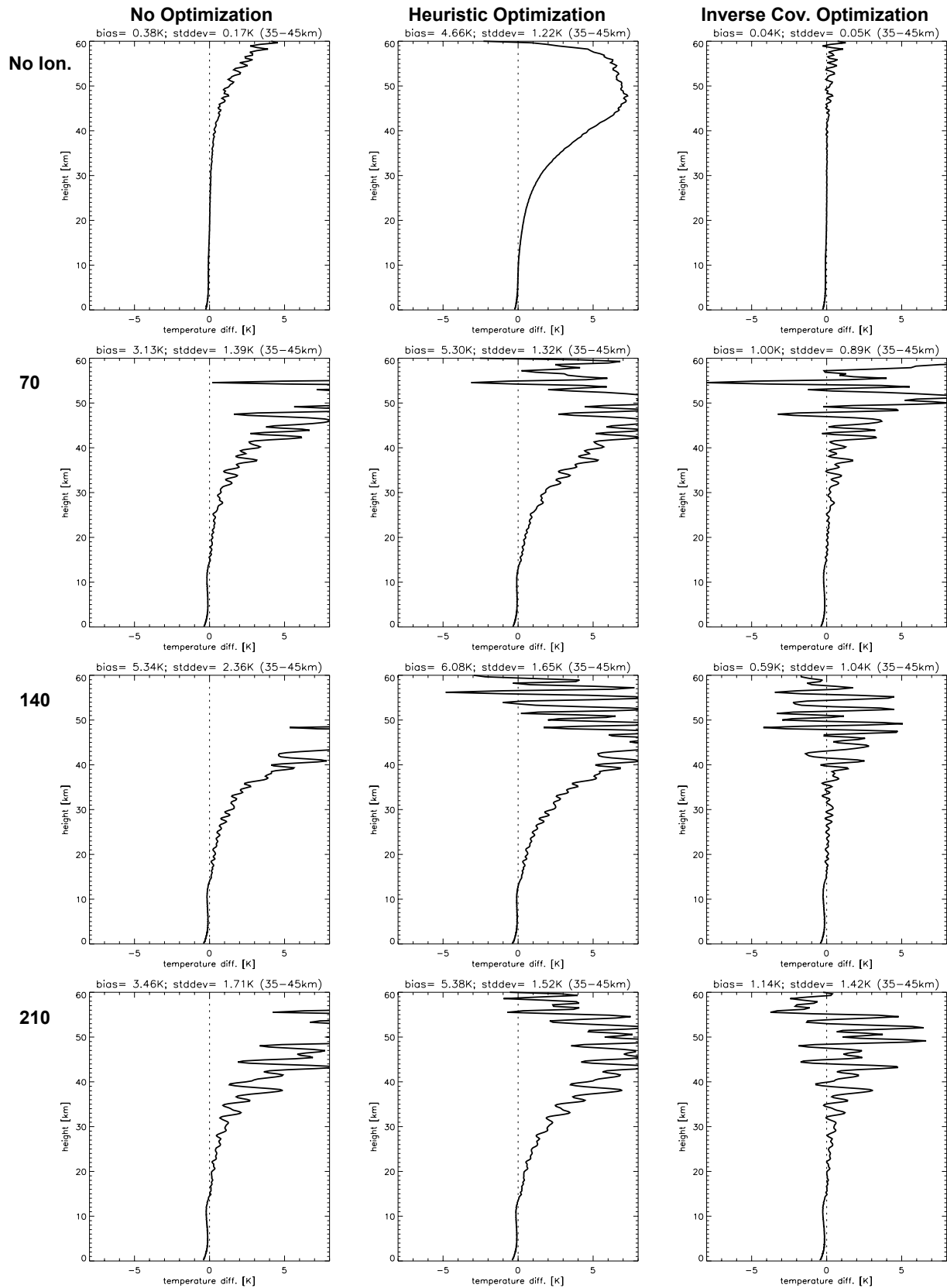


Figure B.5.2: Difference between retrieved and "true" temperature. Event case: Nasty 1 event.

NASTY 2 EVENT

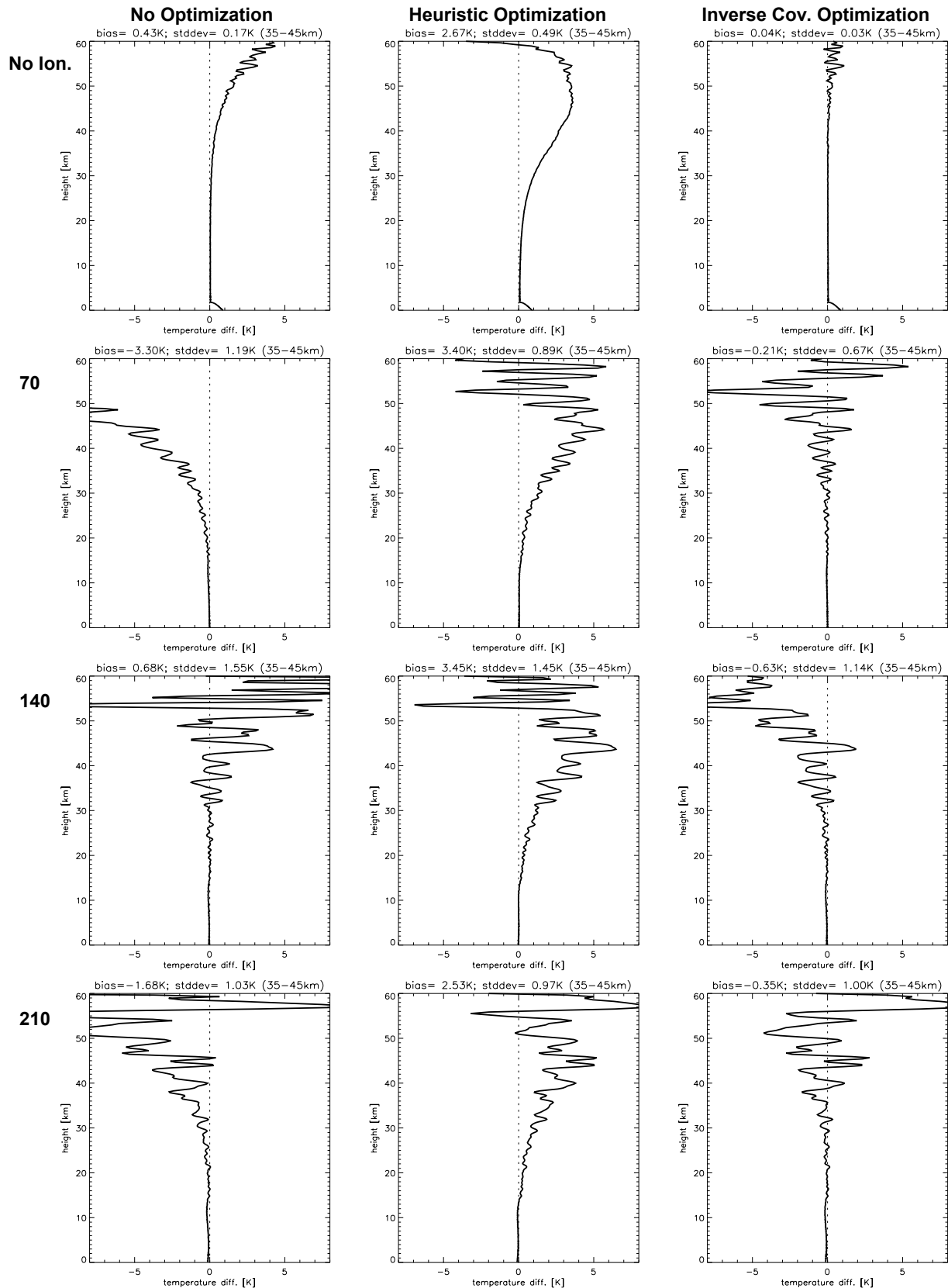


Figure B.5.3: Difference between retrieved and “true” temperature. Event case: Nasty 2 event.

Ω end of document Ω